A novel antiviral lncRNA EDAL shields a T309 *O*-GlcNAcylation site to promote EZH2 degradation

Baokun Sui[1,2,*], Dong Chen[3,4,*], Wei Liu[1,2], Qiong Wu[1,2], Bin Tian[1,2], Jing Hou[3,4], Yingying Li[1,2], Shiyong Liu[5], Juan Xie[5], Hao Jiang[6], Zhaochen Luo[1,2], Lei Lv[1,2], Fei Huang[1,2], Ruiming Li[1,2], Min Cui[1,2], Ming Zhou[1,2], Huanchun Chen[1,2], Zhen F. Fu[1,2,7], Yi Zhang[3,4,†], Ling Zhao[1,2,†]

Running title: lncRNA EDAL inhibits neurotropic viruses

[1] *State Key Laboratory of Agricultural Microbiology, Huazhong Agricultural University, Wuhan, 430070, China;*

[2] *Key Laboratory of Preventive Veterinary Medicine of Hubei Province, College of Veterinary Medicine, Huazhong Agricultural University, Wuhan, 430070, China;*

[3] *Center for Genome analysis and* [4]*Laboratory for Genome Regulation and Human Health, ABLife Inc., Wuhan, 430075, China*

[5] *School of Physics, Huazhong University of Science and Technology, Wuhan, 430074, China;*

[6] *Key Laboratory of Marine Drugs, Ministry of Education, School of Medicine and Pharmacy, Shandong Provincial Key Laboratory of Glycoscience and Glycotechnology, Ocean University of China, Qingdao, 266003, China;*

[7] *Department of Pathology, University of Georgia, Athens, GA 30602, USA;*

[*]These authors contributed equally to this work.

† To whom correspondence should be addressed:

Ling Zhao, Mailing address: State Key Laboratory of Agricultural Microbiology, Huazhong Agricultural University, Wuhan, 430070, China.Tel: +86-27-8728 5016; Fax: +86-27-8728 2608; E-mail: zling604@yahoo.com

Correspondence may also be addressed to

Yi Zhang, Mailing address: Center for Genome analysis and Laboratory for Genome Regulation and Human Health, ABLife Inc., Wuhan, 430075, China. E-mail: yizhang@ablife.cc

Abstract

The central nervous system (CNS) is vulnerable for viral infection, yet few host factors in the CNS are known to defend invasion by neurotropic viruses. We report here that multiple neurotropic viruses, including rabies virus (RABV), vesicular stomatitis virus (VSV), Semliki Forest virus (SFV) and herpes simplex virus 1 (HSV-1), elicit the neuronal expression of a host-encoded lncRNA EDAL. EDAL inhibits the replication of these neurotropic viruses in neuronal cells and RABV infection in mouse brains. EDAL binds to the conserved histone methyltransferase enhancer of zest homolog 2 (EZH2) and specifically causes EZH2 degradation via lysosomes, reducing the cellular H3K27me3 level. The antiviral function of EDAL resides in a 56-nt antiviral substructure through which its 18-nt helix-loop intimately contacts multiple EZH2 sites surrounding T309, a known *O*-GlcNAcylation site. EDAL positively regulate the transcription of *Pcp4l1* encoding a 10 kDa peptide, which inhibits the replication of mutiple neurotropic viruses. Our findings proposed a model in which a neuronal lncRNA can exert an effective antiviral function via blocking a specific *O*-GlcNAcylation that determines EZH2 lysosomal degradation.

Key words: EZH2/lncRNA/neurotropic virus/*O*-GlcNAcylation/PCP4L1

INTRODUCTION

Among infectious diseases of the central nervous system (CNS), those caused by viral pathogens—known as neurotropic viruses—are far more common than bacteria, fungi, and protozoans (2Nd & Mcgavern, 2015, Ludlow, Kortekaas et al., 2016). Neurotropic viruses arrive to the CNS through multiple routes and propagate within various cell types including astrocytes, microglia and neurons, depending on the entering routes and virus types (Manglani & McGavern, 2018). Infection of some neurotropic viruses can cause meningitis or encephalitis and result in severe neurologic dysfunction, such as VSV, SFV, HSV-1 and HIV etc. (Bradshaw & Venkatesan, 2016, Fragkoudis, Dixon-Ballany et al., 2018, Gagnidze, Hajdarovic et al., 2016). Moreover, nearly half of all emerging viruses are neurotropic viruses (Olival & Daszak, 2005), including the Dengue and Zika viruses (Carod-Artal, 2016, Meyding-Lamade & Craemer, 2018). RABV is a typical neurotropic virus and is the causative agent of rabies disease, a globally well-known and often lethal encephalitis. Therefore, it is urgent to develop new approaches for therapies as well as for cheaper and more effective vaccines against rabies (Fisher & Schnell, 2018, Schnell, McGettigan et al., 2010).

Long non-coding RNAs (lncRNAs) are involved in the development, plasticity, and pathology of the nervous system (Batista & Chang, 2013, Briggs, Wolvetang et al., 2015, Fatica & Bozzoni, 2014, Sun, Yang et al., 2017). Notably, around 40% of lncRNAs detected to date are expressed specifically in the brain (Liu, Wang et al., 2017). Genome-wide association studies (GWASs) and functional studies have associated lncRNAs with neurological diseases including autism spectrum disorders (ASD), schizophrenia, Alzheimer's disease, and neuropathic pain, among others (Briggs et al., 2015). Mechanistically, it has been shown that lncRNAs can regulate chromatin modifications and gene expression, at both the transcriptional and the

post-transcriptional levels (Bonasio & Shiekhattar, 2014, Mercer, Dinger et al., 2009, Wang & Chang, 2011). LncRNAs have recently been shown to regulate innate immune responses by either promoting or inhibiting viral genome replication, highlighting them as a class of novel targets for developing antiviral therapies (Carpenter & Fitzgerald, 2018, Fortes & Morris, 2016, Imamura, Imamachi et al., 2014, Kambara, Niazi et al., 2014, Ma, Han et al., 2017, Ouyang, Hu et al., 2016, Ouyang, Zhu et al., 2014). It is conceivable that antiviral lncRNAs targeting none-innate immune response pathway may exist in neuron cells and brains, which has not been documented yet.

Polycomb repressive complex 2 (PRC2) is a protein complex with an epigenetic regulator function in maintaining the histone modifications that mark transcriptional repression states which are established during early developmental stages (Ringrose, 2017). Some lncRNAs are known to interact with and direct PRC2 towards the chromatin sites of action, thusly defining a trans-acting lncRNA mechanism (Jin, Lv et al., 2018, Rinn, Kertesz et al., 2007). The EZH2 methyltransferase enzyme is the catalytic component of PRC2: it binds RNAs and catalyzes di- or tri-methylation of histone H3 lysine 27 (H3K27me2/3), a modification which leads to the formation of facultative heterochromatin and thus to transcriptional repression (Justin, Zhang et al., 2016, Kasinath, Faini et al., 2018, Margueron & Reinberg, 2011). Many cancers are known to feature very high EZH2 expression levels, so this protein has emerged as an anticancer target for which multiple chemical inhibitors have been developed (Kim & Roberts, 2016, Lee, Yu et al., 2018). It has also been recently reported that inhibitors of the histone methyltransferase activity of EZH2 can suppress infection by several viruses, suggesting a function of EZH2 and/or PRC2 in regulating viral infection (Arbuckle, Gardina et al., 2017). However, it is unclear how this regulation occurs. In general, PRC2 (EZH2) binds different classes of RNAs in a promiscuous manner *in vitro* and in cells, and some lncRNAs such as RepA RNA show *in vitro* specificity with PRC2

(Davidovich, Wang et al., 2015a, Davidovich, Zheng et al., 2013). The specificity of PRC2 (EZH2) interaction with lncRNAs is expected for at least some of its regulation and biological function in living cells , which require further studies (Davidovich, Wang et al., 2015b).

Biochemical studies have established that post-translational modifications (PTM) of EZH2, including phosphorylation and *O*-GlcNAcylation, can regulate its stability (Chu, Lo et al., 2014, Lo, Shie et al., 2018, Wu & Zhang, 2011). NIMA-related kinase (NEK2) was recently shown to phosphorylate EZH2, which protects EZH2 from ubiquitin-dependent proteasome degradation, thereby promoting glioblastoma growth and radio-resistance (Wang, Cheng et al., 2017). LncRNAs have been shown to regulate the stability of proteins such as ZMYND8 and CARM1, expanding the scope of their known regulatory functions (Jin, Xu et al., 2019, Qin, Xu et al., 2019). It was recently reported that a newly identified lncRNA (ANCR) increases the phosphorylation-mediated stability of EZH2 by promoting its interaction with the well-known kinase CDK1 (Li, Hou et al., 2017). However, it remains unclear how lncRNA interacts with proteins to regulate their stability.

Here, we report our discovery of a novel virus-inducible lncRNA (EZH2 degradation-associated lncRNA, EDAL) that we identified via deep RNA-seq of RABV-infected Neuro-2a (N2a) cells. EDAL can inhibit the replication of multiple neurotropic viruses in neuronal cells, including two negative strand RNA viruses-RABV and VSV, a positive strand RNA virus-SFV and a DNA virus-HSV-1, as well as RABV infection in mice. We found that increased EDAL levels reduce the cellular level of EZH2 and of its enzymatic product H3K27me3 epigenetic marks. Mutational analysis, structural prediction, and molecular simulations revealed that a 56-nt functional substructure of EDAL, wherein a helical-loop intimately contacts EZH2 T309 and the surrounding regions. This protein-lncRNA interaction prevents T309 from receiving a

previously demonstrated *O*-GlcNAcylation PTM that is known to increase EZH2's cellular stability. We further show that *Pcp4l1* is a EDAL-regulated gene which encodes a small peptide suppressing RABV, VSV, SFV and HSV-1 infection. Thus, our study reveals a previously unknown lncRNA-PTM-mediated link between host antiviral responses and epigenetic regulation.

Results

Identification of a host lncRNA induced by viral infection

We conducted a time-course RNA-seq analysis of cultured N2a cells that were infected with pathogenic RABV (CVS-B2c strain) or were mock infection treated. Subsequently, after a conventional data analysis for differentially expressed mRNA transcripts and a correlation-based analysis to identify time-dependent patterns of transcriptome-wide gene expression changes in response to RABV infection (Appendix Fig S1), we used TopHat2 and Cufflinks (Trapnell, Roberts et al., 2012) to perform a novel lncRNA species prediction, and then conducted a similar differential expression analysis to identify lncRNAs which exhibited significant changes in their accumulation upon RABV infection. This identified 1,434 differentially expressed lncRNAs (Fig 1A). qPCR analysis successfully confirmed the significantly up-regulated expression of ten of the most highly up-regulated of these lncRNAs in response to RABV infection (Fig 1B).

Pursuing the idea that lncRNAs accumulated in response to viral infection may somehow participate in cellular responses to RABV, we cloned six of the strongly up-regulated lncRNAs and overexpressed them in N2a cells; these cells were then infected with pathogenic RABV at a low multiplicity of infection (MOI of 0.01). Excitingly, one of these—XLOC_007537, was predicted to be 1,564 nt in length and to be transcribed from an intergenic locus on

chromosome 11—was found to inhibit RABV infection in N2a cells (Fig 1C and Fig EV1A). The 5' and 3' boundaries of this XLOC_007537 lncRNA were confirmed by 5'- and 3'- RACE experiments (Fig EV2B). This long intergenic non-coding RNA had no obvious annotation hits after examining its sequence using tools available with the NONCODEv5 (Fang, Zhang et al., 2017), lncRNAdb 2.0 (Quek, Thomson et al., 2015), or LNCipedia 5.0 (Volders, Verheggen et al., 2015) databases. Our PhyloCSF analysis (Lin, Jungreis et al., 2011) yielded a score of -498.50 for this candidate lncRNA (Fig EV1C), strongly reinforcing its non-coding characteristics. Since XLOC_007537 was found to cause EZH2 degradation in the following study, we named it as EZH2 degradation-associated lncRNA (EDAL). EDAL is partially conserved among rats, humans, rhesus, and chimps (Fig EV1D). While RNA fluorescence *in situ* hybridization (FISH) analysis of N2a cells revealed that EDAL occurs in both the cytoplasm and the nucleus, the EDAL signal was stronger in the cytoplasm (Fig EV1E).

Neuronal cell specific accumulation of EDAL induced by viral infection

We next conducted experiments wherein N2a cells were infected with RABV at different doses for different periods, and EDAL levels were measured via qPCR over a time course of infection. We found that the extent of EDAL up-regulation was dependent on the MOI used for viral infection (Fig 1D), as well as on the infection duration (Fig 1E): increased MOI and increased duration resulted in an increased extent of up-regulation. Bessides RABV, we found several other neutropic viruses, including another negative strand RNA viruses-VSV (Fig 1F and Fig EV2A), a positive strand RNA virus-SFV (Fig 1G and Fig EV2B) and a DNA virus-HSV-1 (Fig 1H and Fig EV2C), could also induce up-regulation of EDAL in a dose- and time-dependent manner. Additional experiments showed that only RABV viral genomic RNA could induce EDAL accumulation: viral proteins, double-stranded RNA (dsRNA), and

194 interferons did not significantly induce EDAL (Fig 1I and Fig EV2D-G).

195 We then used qPCR to investigate both the basal level and the
196 RABV-induced levels of EDAL in three mouse neuronal cell lines. These
197 experiments revealed that the basal level of EDAL was much higher in N2a
198 cells (neuron cell line) than that in glia cells, including BV2 (microglia cell line)
199 and C8-D1A (astrocyte cell line) cells (Fig 1J). After RABV infection, the level
200 of EDAL in N2a was significantly up-regulated, while no significant change in
201 the EDAL level was detected in BV2 or C8-D1A cells (Fig 1J). Furthermore,
202 EDAL levels were much higher in brains and spinal cords than in the spleen,
203 liver, or lung (Fig 1K).

204 ***EDAL inhibits viral replication***

205 We next transfected N2a cells with pcDNA3.1 plasmid expressing either EDAL
206 (pcDNA-EDAL) or an EDAL-specific small interfering RNA (siEDAL) and then
207 verified that EDAL was appropriately expressed or specifically silenced in N2a
208 cells (Fig EV3A and 3B). We also confirmed that overexpression or silencing of
209 EDAL did not affect cell viability (Fig EV3C and 3D). Next, we transfected N2a
210 cells with the EDAL expression plasmid and then infected them with RABV at
211 12 hours (h) post transfection. The viral titer in the supernatant of
212 RABV-infected cells transfected with the pcDNA-EDAL vector was 8-fold lower
213 than the titer of control cells transfected with the empty vector pcDNA3.1 at 48
214 h post infection (hpi). At 72 hpi, the same trend was apparent, but the
215 difference was 4.5-fold (Fig 2A).

216 The impact of EDAL silencing on virus titer was assessed using direct
217 immunofluorescence assays with an antibody against the RABV N protein,
218 which allowed calculation of the number of living RABV particles according to
219 the number of immunofluorescent foci (Tian, Luo et al., 2016). Excitingly, and
220 consistent with a virus-replication-inhibiting function for EDAL in N2a cells,

when the expression of EDAL was silenced by siEDAL, the RABV titer increased by around 2-fold compared to the siRNA control cells at 48 hpi. (Fig 2B), and the impact of siEDAL silencing was removed by subsequent overexpression of EDAL (Fig 2C). Interestingly, A similar trend of reduced viral titers in cells transfected with the EDAL plasmid was observed in VSV, SFV and HSV-1-infected cells (Fig 2D-F).

To further explore a role for EDAL in somehow inhibiting viral replication, we next developed a series of recombinant viruses for later experiments with live mice. Specifically, we here used a recombinant RABV (rRABV) virus that was derived from the CVS-B2c strain, and used three different viral constructs: unaltered rRABV, rRABV harboring the EDAL sequence (rRABV-EDAL), and rRABV harboring the reverse complement sequence of EDAL (rRABV-revEDAL) (Fig 2G). Virus growth kinetics experiments with N2a cells showed that the virus titer was significantly lower in the rRABV-EDAL infected cells than both the rRABV-infected cells and the rRABV-revEDAL-infected cells (Fig 2H).

We also analyzed the capacity of the recombinant viruses to spread between infected cells and neighboring cells, the infected N2a cells were covered by low melting agar to inhibit the virus release into the supernatant (Tian et al., 2016). The rRABV-EDAL recombinant virus yielded much smaller fluorescent foci than rRABV and rRABV-revEDAL in the neighboring N2a cells (Fig 2I, left) at 48 hpi, and the fluorescent foci we observed in the rRABV-EDAL-infected samples comprised significantly fewer cells than the fluorescent foci present in the rRABV or rRABV-revEDAL samples (Fig. 2I, right).

EDAL reduces RABV pathogenicity in vivo

To investigate the role of EDAL in RABV infection *in vivo*, we compared the

pathogenicity of rRABV, rRABV-EDAL, and rRABV-revEDAL in the C57BL/6 mouse model. Mice were infected intra-nasally (i.n.) with rRABV, rRABV-EDAL, or rRABV-revEDAL (100 FFU). The mice infected with rRABV and rRABV-revEDAL exhibited decreased body weights starting from 7 to 9 days post infection (dpi), and these decreases became significant between 9 and 14 dpi. In contrast, the body weight of mice infected with rRABV-EDAL only exhibited a slight decrease between 10-14 dpi (Fig 3A). Moreover, the rabies symptoms (including weight loss, ruffled fur, body trembling, and paralysis) of the symptomatic rRABV- and rRABV-revEDAL-infected mice appeared at 7 dpi, and became exacerbated until death at 14 dpi, whereas symptomatic mice infected with rRABV-EDAL had only mild symptoms which occurred from 9 to 15 dpi (Fig 3B). Among all mice, 70% of the mice infected with rRABV-EDAL survived, compared with only 20% and 10% survival ratio for rRABV- and rRABV-revEDAL-infected mice, respectively (Fig 3C).

To quantify the viral load in rRABV and rRABV-EDAL infected brains, the RABV *N* mRNA level in different encephalic regions was analyzed by qPCR after i.n. infection with 100 FFU of different viruses. At 12 dpi, we observed dramatically reduced RABV *N* mRNA levels in rRABV-EDAL-infected vs. rRABV-infected mice: specifically, these reductions were observed in the olfactory bulb, cerebrum, cerebellum, and brain stem regions (Fig 3D). Further immunohistochemistry analysis of the RABV P protein (Fig 3E) and CD45-positive cells (Fig 3F) in various brain regions showed that, unlike rRABV-infected brains, almost no viral antigen or virus-induced inflammation could be observed in rRABV-EDAL-infected mouse brains at 12 dpi. Collectively, these results establish that EDAL can dramatically inhibit intranasal-inoculation-induced RABV infection in mice.

EDAL decreases H3K27me3 levels by promoting lysosome-mediated EZH2 degradation

Having demonstrated that RABV infection induces the accumulation of EDAL and established that EDAL can restrict RABV replication *in vitro* and *in vivo*, we were interested in potential mechanism(s) through which EDAL may exert its antiviral effects. We have for some time been interested in the potential contributions of epigenetic regulation on host responses to neurotropic viruses, and we noted that the N2a cells transfected with the pcDNA3.1 plasmid expressing pcDNA-EDAL had significantly decreased levels of histone methylation. Specifically, immunoblotting experiments with an antibody against the H3K27me3 tri-methylation mark revealed that cells with the empty control plasmid had a signal for this histone methylation of the N-terminal tail of the core histone H3 that was 1.35 times as strong as the signal for cells with the pcDNA-EDAL plasmid (Fig 4A).

To confirm an impact specifically from EDAL on the observed reduction in the H3K27me3 tri-methylation level, we evaluated three other lncRNAs from our dataset which were induced by RABV, namely XLOC_023040, ENSMUSG00000087590.2 (ENS_87590.2), and XLOC_059122 mentioned in Fig. 1C. Notably, the expression of these lncRNAs did not change the H3K27me3 tri-methylation level (Fig 4A), strongly supporting the specificity of EDAL in exerting this inhibitory effect. These results led us to speculate that EDAL may interfere with viral replication via alteration of histone methylation.

It is now understood that PRC2 mediates the H3K27me3 tri-methylation process (Simon & Kingston, 2009), so we performed additional immunoblotting with an antibody against EZH2—the enzymatic subunit of PRC2 responsible for its methyl-transferase activity. As with the signal for H3K27me3 tri-methylation, we observed weaker signals for EZH2 in cells with the plasmid for pcDNA-EDAL compared to controls (Fig 4A and B). We next used the recombinant viruses that we used for mice infection (Fig 3) to repeat the above experiments, and the same decreasing trend was observed in N2a cells

infected with the rRABV-EDAL virus (Fig 4C). Moreover, no such decreases in the H3K27me3 tri-methylation signal or the EZH2 protein level were observed upon expression of revEDAL or the three aforementioned lncRNAs (Fig 4C), again highlighting an apparently specific contribution of EDAL to the reduced levels of H3K27me3 and its catalyst EZH2.

To further determine the impact of EDAL on the H3K27me3 tri-methylation signal and/or the EZH2 protein level, N2a cells were transfected with siEDAL. Consistently, silencing of EDAL enhanced the levels of both EZH2 and H3K27me3 in N2a cells (Fig 4D), and overexpression of EDAL counteracted the elevated EZH2 level induced by siEDAL (Fig 4D). Importantly, we also found that the EZH2 protein level, but not the *EZH2* mRNA level, was reduced by EDAL—and noted that expression of revEDAL or other three control lncNRAs did not affect the protein or the mRNA level for EZH2 (Fig 4E)—results clearly suggesting that the impact of EDAL on EZH2 accumulation occurs at the protein level.

We therefore suspected that an EDAL–EZH2 interaction might somehow promote the degradation of EZH2, thereby reducing the overall cellular capacity for its methyltransferase activity, potentially explaining the observed reduction in H3K27me3 tri-methylation. To test this hypothesis, we treated cells with compounds that inhibit the protein degradation functions of proteasomes (MG132) or lysosomes (NH_4Cl), and then assayed the EZH2 protein accumulation and the H3K27me3 tri-methylation level upon EDAL expression. These experiments showed that NH_4Cl but not MG132 treatment restored the EZH2 protein and H3K27me3 tri-methylation levels, results supporting that EDAL somehow causes EZH2 degradation via the lysosomal degradation pathway (Fig 4F).

A 56 nt 5' segment is responsible for EDAL's antiviral activity

Although not necessarily conserved, secondary structures are thus far good

candidates for identification of functional elements of lncRNAs (Bonasio & Shiekhattar, 2014, Johnsson, Lipovich et al., 2014, Mercer & Mattick, 2013, Rivas, Clements et al., 2017). Seeking to identify secondary structures of EDAL that affect its specific interaction with EZH2, predictions using the RNAstructure 5.3 program indicated that EDAL could be divided into four major sub-structures, each containing a number of base-paired structures and hairpin structures (Fig 5A). We cloned the segments corresponding to the four sub-structures (EDAL-1, EDAL-2, etc.) into pcDNA3.1, and then each of the four segments was individually expressed in N2a cells, followed by immunoblotting-based evaluation of the EZH2 protein and H3K27me3 tri-methylation levels. Interestingly, the first truncated segment (EDAL-1) located at the 5' end of EDAL, but none of the other three segments, significantly reduced both the EZH2 and H3K27me3 levels (Fig 5B). Consistent with a specific impact from this EDAL sub-structure, only EDAL-1 restricted RABV replication in N2a cells (Fig 5C).

To pinpoint the specific fragment capable of exerting the antiviral function, EDAL-1 was assessed as four separate truncation segments (EDAL-1 △1-43, EDAL-1 △98-153, EDAL-1 △160-180 and EDAL-1 △207-303) (prepared as depicted in Fig 5D). Each of the EDAL-1 variants were assessed in N2a cells: only EDAL-1 △98-153 failed to decrease the EZH2 and H3K27me3 levels and failed to inhibit rRABV replication (Fig 5E and F).

To confirm that EDAL 98-153 nt can inhibit RABV infection, this 56 nt segment was expressed by itself and as a fusion with the 3' end of the three aforementioned lncRNAs (i.e., from our experiments to successfully demonstrate the specificity of EDAL's antiviral effects) (Fig 5G). As expected, the fragment alone and the three fusion lncRNAs reduced the EZH2 and H3K27me3 levels (Fig 5H) and also reduced RABV replication (Fig 5I). These results establish that the 56 nt segment at the 98-153 position of the 5' end of

EDAL is essential for the EZH2-mediated antiviral effects we observed in neuronal cells.

EDAL reduces EZH2 stability by impeding an O-GlcNAcylation PTM at the T309 site

Previous studies have revealed that phosphorylation and *O*-GlcNAcylation can influence the stability of EZH2 (Chu et al., 2014, Lo et al., 2018, Wu & Zhang, 2011). At least two phosphorylation sites among human EZH2, T345 and T487, were shown to affect its stability (Wu & Zhang, 2011). However, we found that EDAL could still cause the degradation of murine EZH2 when the corresponding phosphorylation sites were mutated to T341A and T485A, (Fig EV4A), indicating that EDAL does not apparently impair the phosphorylation of EZH2.

There are five known *O*-GlcNAcylation sites (S73, S76, S84, T313, and S729) in human EZH2 that can regulate EZH2 stability and enzymatic activity (Chu et al., 2014, Lo et al., 2018). Based on the sequence alignment between human and murine EZH2, we found that S73, S75, T309, and S725 are potential *O*-GlcNAcylation sites of murine EZH2 (Fig EV4B). We mutated each of the potential *O*-GlcNAcylation sites of murine EZH2 and then co-transfected these mutant variants together with pcDNA3.1, pcDNA-EDAL, or pcDNA-revEDAL in N2a cells. We found only T309A mutation lost the EDAL-promoted EZH2 degradation (Fig 6A), while there was no significant difference in the extent of degradation among the wild type, S73A, S75A, or S725A variants of EZH2 (Fig 6A). We observed the same trends for EZH2 variants bearing multiple mutations: a S73/S75/S725 triple-alanine-mutant did not affect EDAL-promoted EZH2 degradation, whereas EDAL lost its impact on the degradation of a tetra-alanine EZH2 variant with mutation of position 309 (Fig 6B). These results together indicated that EDAL mediated EZH2 degradation via specifically blocking T309 *O*-GlcNAcylation site.

In order to further pursue the EDAL-EZH2 interactions which may contribute to the EDAL specific blocking of the EZH2 T309 *O*-GlcNAcylation, we decided to predict the interaction sites between the 56-nt antiviral EDAL substructure and EZH2. RNA tertiary structure prediction revealed a tertiary structure for the 56-nt antiviral RNA segment: the helix-loop tertiary structure folded by the 18-nt terminal hairpin corresponding to 125-142 of EDAL was packed on the second helix folded by the stem base-paired structure, and most of the two structural components were free for contacting other partners (Fig 6C). We then conducted for molecular docking using the 3dRPC program taking the advantage of recently published tertiary structures for EZH2 (Huang, Li et al., 2016, Huang, Li et al., 2018, Justin et al., 2016, Kasinath et al., 2018). Among the top scored structures, one showing that the 18-nt terminal helix-loop tertiary structure was intimately interacted with EZH2 residues at positions 271-274, 280-283, 305-308, 310-312, and 451-454 (Fig 6C). To validate these predicted interactions, we mutated all these EDAL interacting residues in EZH2 to alanine (A). We co-transfected N2a cells with plasmids expressing wild type EZH2 and EZH2 mutant variants together with the pcDNA3.1, pcDNA-EDAL or pcDNA-revEDAL plasmids. The results revealed a striking difference: in the presence of EDAL, there was no obvious reduction in the levels of the EZH2 variants bearing alanine substitution mutations at the 271-274, 280-283, or 305-308 positions, whereas there was obvious degradation of WT EZH2 and the other variants (Fig 6D). Thus, the cellular stability of EZH2 is directly affected by an interaction between EDAL and the EZH2 residues at positions 271-274, 280-283, and 305-308. Previous studies have demonstrated that the binding region between human EZH2 and many reported lncRNAs was the segment of 343-368 aa (Kaneko, Li et al., 2010), and the corresponding region in murine EZH2 was between 338 and 364 aa determined by sequence comparison. However, our results indicate that EDAL binds to murine EZH2 in the region of 271-274, 280-283 and 305-308. In order

417 to verify these binding sites between murine EZH2 and EDAL, we truncated
418 murine EZH2 into 1-337aa and cloned the truncated fragment into pCAGGS
419 vector. Then we confirmed that the specific EDAL interaction sites on EZH2
420 are in its N-terminal region (1-337 aa) using an RNA pull-down analysis (Fig
421 6E). Reciprocally, the expression of an EDAL variant lacking the 18-nt terminal
422 hairpin segment (125-142 nt) lost the ability to promote the degradation of both
423 over-expressed and endogenous EZH2 (Fig 6F).

424 The molecular docking and validation experiments supported a model that
425 EDAL can specifically binds to EZH2 at T309 *O*-GlcNAcylation site. We
426 therefore speculated that EDAL binding might impair the *O*-GlcNAcylation at
427 T309 site, potentially preventing an EZH2-stability-promoting effect associated
428 with this PTM. Pursuing this, we evaluated the effect of EDAL expression on
429 the *O*-GlcNAcylation level of EZH2 at the T309 site. To exclude the impact of
430 other *O*-GlcNAcylation sites on the detected level of EZH2 *O*-GlcNAcylation,
431 pCAGGS-EZH2-S73/S75/S725A-flag plasmid was transfected together with
432 pcDNA3.1, pcDNA-EDAL, or pcDNA-revEDAL into N2a cells, and then the
433 *O*-GlcNAcylation level on the EZH2-S73/S75/S725A-flag fusion protein was
434 measured post treatment with NH_4Cl. Interestingly, we found that expression of
435 EDAL dramatically reduced the *O*-GlcNAcylation level of EZH2 (Fig 6G).
436 These results support that EDAL specifically contacts T309, shielding T309
437 from *O*-GlcNAcylation.

438 ***The EZH2 inhibitor gsk126 protects neuronal cells from viral infection***

439 If EDAL's antiviral effects are indeed mediated by its reduced EZH2
440 methyltransferase activity, then we could anticipate that chemical inhibition of
441 EZH2 should cause antiviral effects. Gsk126 is a specific inhibitor of EZH2
442 methyltransferase activity (Mccabe, Ott et al., 2012), and we evaluated the
443 effects of gsk126 on RABV and VSV replication in N2a cells. After testing
444 toxicity (Appendix FigS2A) and identifying a suitable working concentration of

gsk126 (Appendix Fig S2B), we pretreated N2a cells with 4 μmol (μM) gsk126 and then infected them with rRABV, or VSV. The replication of both rRABV (Appendix Fig S2C) and VSV (Appendix Fig S2D) was significantly decreased by treatment with gsk126, results which reinforce a specific role for EZH2's methyltransferase activity on the antiviral effects we observed in N2a cells and which demonstrate proof-of-concept for a therapeutic strategy against a neurotropic virus.

EDAL restricts viral replication by up-regulation of an antiviral peptide PCP4L1

Next we attempt to identify the genes which might be up-regulated by EDAL via decreasing H3K27me3 levels. N2a cells were transfected with pcDNA-EDAL or pcDNA3.1, and then infected with RABV at MOI 1. At 48 hpi, the poly(A)-RNA was isolated for deep sequencing. A cut-off of 0.05 FDR resulted in a total of 75 up-regulated genes (Fig 7A). We next wanted to identify the direct EDAL targets among genes regulated by EDAL *in trans*. We turned our attention to the altered H3K27me3 modification as an additional selection criterion for EDAL to induce EZH2 degradation and reduce H3K27me3 level. Chromatin Immunoprecipitation Sequencing (ChIP-seq) was performed by using anti-H3K27me3 antibody to profile the distribution of H3K27me3 marks on the genome of N2a cells upon transfection with pcDNA-EDAL or control plasmids, and then the data were summarized in Appendix Table S1. Analysis of H3K27me3 peaks indicative of the epigenetic silencing positions revealed many fewer peaks—11,918 vs. 59,706—in EDAL overexpressed samples compared with the samples transfected with empty control plasmids, consistent with the EDAL-reduced cellular level of H3K27me3. In total, 2026 genes lost H3K27me3 mark and only 167 genes gained after EDAL overexpression (Fig 7B). Most EDAL-upregulated genes naturally did not contain H3K27me3 mark, consistent with a recent report that many H3K27me3 marks in adult mice is not related to transcriptional regulation

(Jadhav, Nalapareddy et al., 2016).

The EDAL-response genes with up-regulated transcription and the loss of H3K27me3 mark should represent candidate genes whose expression was subjected to the EDAL-EZH2 regulation, which we considered for further investigation. Six such genes were selected and evaluated whether they could restrict RABV replication. These genes were overexpressed by transient transfection in N2a cells and then RABV was infected at 12 h later. The supernatant was collect at 48 hpi and the virus titers in cell supernatant were measured. The results demonstrated that the gene encoding purkinje cell protein 4-like 1 (PCP4L1), which is small neuronal IQ motif protein closely related to the calmodulin-binding protein PCP4/PEP-19 (Bulfone, Caccioppoli et al., 2004, Morgan & Morgan, 2012), could significantly inhibit RABV replication (Fig 7C). By transfecting different amount of the plasmid expressing PCP4L1 in N2a cells, we found that PCP4L1 could inhibit RABV replication in a dose-dependent manner (Fig 7D). Furthermore, we found that PCP4L1 overexpression reduced RABV N protein level (Fig 7E), and also the virus titers of VSV, SFV and HSV-1 in N2a cells (Fig 7F-H).

ChIP-seq results showed that the H3K27me3 level on the promoter region of *Pcp4l1* was dramatically decreased after EDAL overexpression (Fig 7I), which was validated by ChIP-qPCR assay (Fig 7J). After treatment with EZH2's inhibitor gsk126, the transcriptional level of *Pcp4l1* was significantly increased, confirming that *Pcp4l1* transcription is regulated by EZH2 (Fig 7K). All these results together suggest that EDAL might promote PCP4L1 expression by down-regulating the EZH2-mediated H3K27me3 deposition.

DISCUSSION

We report here that multiple neurotropic viruses elicit the expression of a host lncRNA EDAL. EDAL inhibits the replication of RABV, VSV, SFV and HSV-1 in

neuronal cells, and suppresses RABV infection in mouse brains. EDAL binds to the histone methyltransferase EZH2, a widely conserved epigenetic regulator, and specifically causes EZH2's lysosomal degradation by blocking T309 *O*-GlcNAcylation. This in turn reduces cellular H3K27me3 levels. EDAL's antiviral function resides in a 56-nt antiviral substructure that can fold into a tertiary structure with a 18-nt helix-loop that intimately contacts the T309 *O*-GlcNAcylation site of EZH2. Mutation analysis confirmed that EDAL's effect on lysosomal EZH2 degradation requires the interaction between the 18 nt helix-loop of EDAL and EZH2 sites surrounding T309 *O*-GlcNAcylation, supporting that EDAL blocks a specific EZH2 PTM via tertiary interactions. Additionally, EDAL antiviral function could be attributed to its activated expression of a novel antiviral small peptide PCP4L1. Our discovery that neurotropicviruses elicit the expression of a neuronal antiviral lncRNA which facilitates the key epigenetic regulator EZH2 toward lysosomal degradation illustrates a way for a low level of lncRNA to effectively reduce the level of its target protein, as well as a direct biomolecular link among virus infection, host antiviral responses, and epigenetic regulation (Fig 7L). The findings of the antiviral and EZH2 degradation function carried by a 56-nt segment of EDAL and its predicted capability of folding into a functional tertiary structure together highlight a mechanism for the specificity of lncRNA actions (Fig 6C).

Recent studies have shown that post-translational modification (PTM) of EZH2 by phosphorylation affects its stability. CDK1 phosphorylates human EZH2 at T345 and T487, promoting ubiquitination of EZH2 and its subsequent degradation in proteasomes (Kaneko et al., 2010, Wu & Zhang, 2011). T345 phosphorylation site is involved in regulating EZH2 binding with HOTAIR and XIST lncRNA (Kaneko et al., 2010). K348 acetylation reduces the phosphorylation of EZH2 at T345 and T487, and increases the stability of EZH2 without interrupting PRC2 formation (Wan, Zhan et al., 2015). LncRNA ANCR facilitates the CDK1-EZH2 interaction and enhances the

phosphorylation at T345 and T487, leading to EZH2 degradation and the attenuation of the invasion and metastasis of breast cancer (Li et al., 2017).

It has been recently shown that *O*-GlcNAcylation catalyzed by *O*-linked N-acetylglucosaminyltransferase (OGT) occurs at S73, S76, S84, T313, and S729 sites of the human EZH2, which does not affect the formation of the PRC2 complex. S76 and T313 are conserved in mammals, and S76A and T313A mutations independently reduce the stability of EZH2 (Chu et al., 2014, Lo et al., 2018). In the present study, molecular docking indicated that a 56-nt functional domain of EDAL lncRNA conveying both the antiviral and EZH2 degradation activity can shield T309 of mouse EZH2, the analogue of T313 in human EZH2, from the *O*-GlcNAcylation modification. PTM of biologically and therapeutically important proteins by *O*-GlcNAcylation are of interest as both lncRNA targets and as therapeutic targets. *O*-GlcNAcylation is highly abundant in eukaryotes, occurring in both the nucleus and the cytoplasm (Hanover, Krause et al., 2012, Hart, Slawson et al., 2011, Lewis & Hanover, 2014). In light of our confirmation of EDAL's regulation of EZH2 *O*-GlcNAcylation, lncRNA regulation of other *O*-GlcNAcylation modification sites on other target regulatory (and other) proteins can be anticipated.

Note that EZH2-lncRNA interactions have been a popular model for studies of epigenetic silencing by PRC2 (Davidovich & Cech, 2015, Lee, 2012, Margueron & Reinberg, 2011, Mercer & Mattick, 2013, N, 2013, Ringrose, 2017). However, the binding specificity of PRC2 for lncRNAs and other transcripts has been challenged and re-examined recently, leading to controversy about binding specificity and promiscuity (Davidovich et al., 2015b, Davidovich et al., 2013, Wang, Goodrich et al., 2017). Our findings indicated that EDAL binds to EZH2 at a site different from that of lncRNA-HOTAIR binding of human EZH2 via residues in 342-368 region (Kaneko et al., 2010). More importantly, this study has shown that a 56-nt EDAL segment

559 independently carries both the antiviral and EZH2 degradation function.
560 Although we have not yet obtained structural data to support its predicted
561 structure, our data for the function of the intimate contacts between the 18-nt
562 helix-loop of EDAL and EZH2's T309 *O*-GlcNAcylation site offers a new
563 example of EZH2-lncRNA recognition and specificity.

564 DNA viral genome-encoded lncRNAs have recently been shown to actively
565 interact with host epigenetic machinery to regulate both their own and host
566 chromatin structure dynamics (Scott, 2017). Some DNA viruses repress
567 transcription and stabilize viral latency by methylating their host's genomic
568 DNA (Knipe, Raja et al., 2017, Lieberman, 2016). In plants, both RNA and DNA
569 viruses encode suppressors that limit the silencing capability of the host plants
570 (Buchmann, Asad et al., 2009, Ruiz-Ferrer & Voinnet, 2009, Yang, Fang et al.,
571 2013, Zhang, Chen et al., 2011). These silencing suppressors also reduce
572 RNA-directed DNA methylation activity at transposons and repetitive
573 sequences in the host genome, suggesting a potential regulatory role that
574 plant viruses impose on their host epigenetic dynamics (Buchmann et al., 2009,
575 Romanel, Silva et al., 2012, Zhang et al., 2011).

576 The present study reveals that neurotropic viruses elicits the expression of
577 EDAL, a host cell lncRNA which restricts the replication of RABV, VSV, SFV
578 and HSV-1. We experimentally link EDAL's antiviral activity to its function in
579 decreasing the cellular stability of EZH2, a protein whose antiviral activity has
580 been recently revealed against the DNA virus HSV-1 (Arbuckle et al., 2017).
581 Consequently, we found that the cellular level of H3K27me3 marks was
582 reduced in neuronal cells, which was accompanied by the removal of in the
583 enriched H3K27me3 mark in an antiviral gene *Pcp4l1* (Fig 7L). These findings
584 suggest that viruses can elicit the expression of a host lncRNA which mediates
585 EZH2 destabilization and reprograms host chromatin structure dynamics. This
586 regulation could be anticipated during the infection by other RNA viruses and

DNA virus as well. Alteration of the host epigenetic dynamics by virus-elicited host lncRNAs might not be limited to EZH2 and H3K27me3 mark. In *Drosophila*, the null mutants of the histone H3 lysine 9 methyltransferase G9a are more sensitive to RNA virus infection, and G9a controls the epigenetic state of immunity genes (Kramer, Kochinke et al., 2011, Merkling, Bronkhorst et al., 2015). It is thus possible that lncRNAs may be involved in G9a-regulated RNA virus responses.

Expression of thousands of lncRNAs has been shown to respond to DNA and RNA virus infection (Ouyang et al., 2016). Some of these lncRNAs have been shown to regulate antiviral immunity via targeting transcription factors and modulating histone modification. For example, lnc-DC binds directly to STAT3 in the cytoplasm, acting as a molecular shield to prevent STAT3 from binding to and de-phosphorylation by SHP1. As a result, lnc-DC indirectly promotes STAT3 phosphorylation on tyrosine-705 and controls human dendritic cell differentiation (Wang, Xue et al., 2014). Both mechanisms lead to the altered expression of cytokines, including IFN and TNF, as well as antiviral proteins from interferon-stimulated genes (ISGs) (Ouyang et al., 2016). It has been shown that lnc-Lsm3b binds to viral RNA sensor RIG-I as a molecular decoy, which inactive RIG-I at the late stage of viral infection and blocks type I IFN responses (Jiang, Zhang et al., 2018). Additionally, Lnczc3h7a serves as a molecular scaffold to stabilize RIG-I-TRIM25 complex and facilitates TRIM25-mediated ubiquitination of RIG-I, which promotes antiviral innate immune responses (Lin, Jiang et al., 2019). The results from EDAL in this study define epigenetic regulators as effective targets of lncRNAs in antiviral responses.

PCP4L1 is a 68 amino acids polypeptide which display sequence similarity to the Purkinje Cell Protein 4 gene (*Pcp4*) and both of which are characterized by their C-terminal IQ domain ends (Bulfone et al., 2004). PCP4L1 display a

615 distinct expression pattern which is dominantly expressed in the CNS, and
616 mostly expressed in circumventricular organs and modulate the production of
617 the cerebrospinal fluid in the adult brain (Bulfone et al., 2004). Previous studies
618 showed that PCP4L1 may be a latent calmodulin binding protein which
619 becomes activated by post-translational modification (Morgan & Morgan,
620 2012). Here we demonstrate that PCP4L1 could inhibit multiple neurotropic
621 virus infection in neuronal cells. Our results therefore reveal a novel antiviral
622 protein which preventing the invasion of RABV, VSV, SFV, HSV-1 and maybe
623 other neurotropic viruses into CNS.

624 In summary, our study of a major neurotropic virus reveals a previously
625 unknown lncRNA-EZH2 PTM-mediated link between host antiviral responses
626 and epigenetic regulation, and the involvement of a high specificity of
627 lncRNA-protein tertiary interaction. The findings may reshape the current
628 understanding of the lncRNA regulatory function, mechanism and its
629 partnership with EZH2. EZH2 is a promising anticancer target with a
630 well-established oncogenic role in a large variety of cancers (Conway, Healy et
631 al., 2015, Kim & Roberts, 2016). The anticancer activities of a number of EZH2
632 inhibitor compounds have been reported (Kim & Roberts, 2016, Mccabe et al.,
633 2012). The exciting finding of the 56-nt RNA substructure carrying the full
634 EZH2 inhibitor function not only offers an example of EZH2-lncRNA
635 recognition and specificity, but also provides new opportunity for developing
636 anticancer and antiviral therapeutics, as well as for developing molecular
637 tracers of EZH2 to explore the cellular activity of EZH2 during its life time.

638

639

640

641

642 ## Materials and Methods

643 ### Cell lines, viruses, and mice

644 Cell lines N2a (murine neuroblastoma N2a cells, ATCC® CCL-131), BSR (a
645 clone of BHK-21, ATCC®CCL-10), C8-D1A (murine astrocytes,
646 ATCC®CRL-2541) and Vero (*Cercopithecus aethiops* kidney cells,
647 ATCC®CCL-81) were obtained from American Type Culture Collection. BV2
648 (murine microglia, BNCC337749) were obtained from BeNa Culture Collection.
649 Cells grown in a 37°C humidified 5% CO_2 atmosphere, growth media was
650 DMEM or RPMI1640 supplemented with 10% (vol/vol) FBS (Gibco) and 1%
651 antibiotics (penicillin and streptomycin) (Beyotime). The recombinant rRABVs
652 were cloned from RABV strain challenge virus standard-B2c (CVS-B2c) and
653 constructed as described previously (Tian et al., 2016). VSV is propagated in
654 BHK-21 cells and stored in our lab. SFV and HSV-1 is a gift from Dr. Bo Zhang
655 (Wuhan Institute of Virology, Chinese Academy of Sciences, Wuhan, China)
656 and Dr. Gang Cao (Huazhong Agricultural University, China), respectively, both
657 of which are propagated in Vero cells. Female C57BL/6 mice (8 week old) mice
658 were purchased from Hubei Center for Disease Control and Prevention, Hubei,
659 China and housed in the animal facility at Huazhong Agricultural University in
660 accordance with the recommendations in the Guide for the Care and Use of
661 Laboratory Animals of Hubei Province, China. All experimental procedures
662 involving animals were reviewed and approved by The Scientific Ethic
663 Committee of Huazhong Agricultural University (permit No.
664 HZAUMO-2016-009).

665 ### Viral infection

666 Cells (N2a, BV2, C8-D1A and Vero) were infected with different rRABVs, VSV,
667 SFV or HSV-1 at a multiplicity of infection (MOI) of 0.01, 0.1, 1 or 3. After 1 h at
668 37°C, the supernatant was discarded and cells were washed three times with

669 PBS then cultured in DMEM or RPMI1640 supplemented with 2% (vol/vol)
670 FBS (Gibco) and 1% antibiotics (penicillin and streptomycin，Beyotime) at
671 34°C in a humidified 5% CO_2 atmosphere.

672 **RNA-seq library construction, sequencing and lncRNA prediction**
673 **pipeline**

674 Total RNA from RABV infected N2a cells or mock-infected cells were isolated
675 by using Trizol® reagent (Ambion) following the manufacturer's instructions,
676 and then treated with RQ1 DNase (Promega) to remove DNA. RNA quality and
677 quantity were determined by measuring absorbance at 260 nm/280 nm
678 (A260/A280) using a SmartSpec Plus spectrophotometer (BioRad). RNA
679 integrity was verified by subjecting a sample of the RNA to electrophoresis in a
680 1.5% agarose gel.

681 Each RNA-seq library was prepared using 5 μg of total RNA.
682 Polyadenylated mRNAs were purified and concentrated with oligo
683 (dT)-conjugated magnetic beads (Invitrogen) and then used as templates for
684 directional RNA-seq library preparation. Purified RNAs were iron fragmented
685 at 95°C, followed by end repair and 5' adaptor ligation. Reverse transcription
686 was performed using RT primers harboring a 3' adaptor sequence and
687 randomized hexamer. The cDNAs were purified, amplified by PCR, and
688 products 200–500 bp in length were isolated, quantified, and used for
689 sequencing.

690 For high-throughput sequencing, the libraries were prepared following the
691 manufacturer's instructions and analyzed using the Illumina NextSeq500
692 system for 150 nt pair-end sequencing (ABlife. Inc, Wuhan, China).

693 **RNA-seq data processing and alignment**

694 Raw reads containing more than two unknown (N) bases were discarded.
695 Adaptors were removed from the remaining reads, and then short reads (less

than 16 nt in length) and low quality reads (containing more than 20 low quality bases), were also excluded by using the FASTX-Toolkit sequence processing pipeline (Version 0.0.13, http://hannonlab.cshl.edu/fastx_toolkit/) to yield the final data set (clean reads). The *mus musculus* genome sequence (GRCm38) and annotation file (gencode.vM6 basic annotation) were obtained from the GENCODE database (Mudge & Harrow, 2015). Clean reads were aligned end-to-end to the mouse genome by TopHat2 (Kim, Pertea et al., 2013), allowing 2 mismatches. Reads that aligned to more than one genomic location were discarded, and uniquely localized reads were used to calculate the number of reads and RPKM values (RPKM represents reads per kilobase and per million) for each gene. Other statistics, such as gene coverage and depth, and read distribution around transcription start sites (TSSs) and transcription terminal sites (TTSs) were also obtained.

After calculating the expression levels for all genes in the samples, differentially expressed genes (DEGs) between samples were identified by edgeR (Robinson & Oshlack, 2010) using the TMM normalization method (Li, Witten et al., 2012) . For each gene, the fold changes, *p-values*, and adjusted *p-values* (FDR) were also determined by the edgeR package. Genes with FDR < 0.05 were classified as DEGs.

LncRNA prediction pipeline

The lncRNA prediction pipeline was implemented following the methods described by Liu *et al.*(Liu et al., 2017) . The detailed descriptions of the prediction pipeline and filtering thresholds are as follows:

(1) First, using the aligned RNA-seq data (see above), transcripts were assembled by Cufflinks V2.2.1 (Trapnell et al., 2012) using default parameters. After the initial assembly, transcripts with FPKM greater than or equal to 0.1 were subjected to a series of filters.

(2) Cuffcompare (embedded in Cufflinks) was used to compare the transcripts with known mouse genes. Novel transcripts, including those that were intronic, intergenic, and antisense, were retained as candidate lncRNAs. Transcripts within 1000 bp of known coding genes were regarded as UTRs and discarded.

(3) To remove potential protein-coding transcripts, coding potential score (CPS) was evaluated using the Coding Potential Calculator (CPC) (Kong, Zhang et al., 2007) . CPC is a support vector machine-based classifier that assesses the protein-coding potential of transcripts based on six biologically meaningful sequence features. Transcripts with CPS scores below zero were regarded as non-coding RNAs.

(4) Transcripts satisfying the above conditions, containing multiple exons and no fewer than 200 bases, or containing a single exon and no fewer than 1000 bases, were considered to be candidate lncRNAs.

(5) We used Cuffmerge (from Cufflinks) to merge lncRNAs from all samples together to obtain the final lncRNA set. A total of 1662 novel lncRNA transcripts were identified, originating from 1377 lncRNA loci. The expression level of each lncRNA gene was recalculated, and antisense reads of lncRNAs were discarded.

(6) Novel and known lncRNAs were combined into a single data set and subjected to analysis to identify differentially expressed lncRNA, using the same methods used to identify differentially expressed protein coding genes.

Quantitative real-time PCR (qPCR)

Total RNA was isolated from cells and tissues by using Trizol® reagent (Invitrogen). The genomic DNA was eliminated with TURBO DNA-free™ Kit (Ambion, AM1907) as the manufacturer's instructions. RNA quality was assessed by using NanoDrop 2000 (Thermo Scientific). The cDNAs were synthesized by ReverTra Ace qPCR RT Master Mix (Toyobo, FSQ-201) or

First-Strand cDNA Synthesis Kit (Toyobo, FSK-101). qPCR was performed using SYBR Green Supermix (Bio-Rad). Primer sequences used in this study were listed in Appendix Table S2.

Transfections

After seeding, cells were incubated for 12 h at 37°C. Plasmids or siRNA were transfected into cells by using Lipofectamine 3000 (Invitrogen) according to the manufacturer's instruction.

Rapid amplification of cloned cDNA ends (RACE)

Total RNA from N2a cells was isolated by using Trizol® reagent (Invitrogen) and 5'- or 3'- RACE was performed with SMARTer®RACE 5'/3' Kit (Takara, 634858) following the manufacturer's instructions. Primers used for 5'- or 3'-RACE was designed based on the known sequence information. 5' specific primer-GGGCTGGAGAAGTGGTTCCGTTGCTAAGGGTATTCCC; 3' specific primer-GGGAATACCCTTAGCAACGGAACCACTTCTCCAGCC.

Fluorescent *in situ* hybridization

The red fluorescence labeled probe (Ribo-lncRNA FISH Probe Mix) against EDAL lncRNA was designed by Ribobio Co (Guangzhou, China) and was detected by Fluorescent *In Situ* Hybridization Kit (Ribobio, R11060.1) according to the manufacturer's instructions. Briefly, N2a cells grown on cover slips in 24-well plates were fixed with 4% (v/v) paraformaldehyde for 10 minutes (min) at room temperature then washed three times with cold PBS. And the cells were permeabilized in PBS containing 0.5% Triton X-100 for 5 min in 4°C, then blocked in pre-hybridization buffer for 30 min at 37°C. Cells were then incubated with hybridization buffer containing probe overnight at 37°C away from light. After hybridization, cells were washed in the dark with washing buffer (4×SSC/2×SSC/1×SSC) then stained with DAPI for 10 min.

Cells were again washed three times with PBS, and then imaged with an Olympus FV10 laser-scanning confocal microscope.

EDAL specific siRNA

EDAL specific siRNA was designed and synthesized by Ribobio Co. The target sequence was 5'-GGTAGACACCCAGTGACAA-3', and siEDAL sequence was 5'-GGUAGACACCCAGUGACAA -3'.

Cell viability assay

N2a cells were transfected with plasmids, siRNAs or treated with EZH2 specific inhibitor gsk126 (Apexbio, A3446) for indicated time. The viability of N2a cells was evaluated by Cell Titer 96 AQueous One Solution cell proliferation assay kits (Promega, G3582) according to the manufacturer's instruction.

Construction of the recombinant RABVs (rRABV)

Mouse lncRNAs, reverse EDAL (revEDAL) were amplified from the total RNA extracted from RABV-infected N2a cells using the ReverTra Ace qPCR RT Master Mix (TOYOBO, FSQ-201) with Phanta Max Super-Fidelity DNA polymerase (Vazyme, P505-d1). The primer sets used were designed by Primer 6 (PREMIER Biosoft Biolabs) (Appendix Table S2). PCR products were digested with *BsiW*I and *Nhe*I (New England Biolabs) then ligated into the genome of recombinant RABV strain B2c (rB2c) digest used the same enzymes as previously described (Tian et al., 2016).

Rescue of rRABVs

Recombinant RABVs were rescued as reported previously (Tian et al., 2016) . Briefly, BSR cells were transfected with 2 μg of a fully infectious clone, 0.5 μg of pcDNA-N, 0.25 μg of pcDNA-P, 0.15 μg of pcDNA-G, and 0.1 μg of pcDNA-L using Lipo3000 transfection reagent (Invitrogen) according to the

802 manufacturer's instruction. Four days post transfection, supernatants was
803 harvested and examined for the presence of rescued viruses using
804 FITC-conjugated anti-RABV N antibodies (Fujirebio Diagnostics, Malvern, PA).

805 **Virus titration**

806 To determine rRABV and VSV titers, BSR cells were infected with serial
807 dilutions of the viruses. After 1 h incubation in 37°C, the cell supernatant was
808 discarded and washed once with PBS, and then overlaid with DMEM
809 containing 1% low melting point agarose (VWR, 2787C340). After incubation in
810 34°C for 72 h, the cells were stained with FITC-conjugated anti-RABV N
811 antibody (Fujirebio Diagnostics, Malvern, PA). Then the fluorescent foci were
812 counted under a fluorescence microscope. For VSV titration, the plaques were
813 counted at 48 h post infection.

814 For SFV and HSV-1 titration, Vero cells were seeded in 12-well plates and
815 infected with serial dilutions of the viruses. After 1 h incubation in 37°C, the cell
816 supernatant was discarded and washed once with PBS, and then overlaid with
817 DMEM containing 1% low melting point agarose. After incubation in 34°C for
818 48 h, the agarose were removed and then fixed and stained with a solution of
819 0.1% crystal violet and 10% formalin in PBS under UV light. After staining for 4
820 h, the plates were washed with water, and the plaques were counted.

821 **Mouse infection**

822 Eight-week-old female C57BL/6 mice were randomly divided into indicated
823 groups and infected intranasally with rRABV, rRABV-EDAL, rRABV-revEDAL
824 (100 FFU) or mock infected with DMEM in a volume of 20 µl. When moribund,
825 the mice were euthanized with CO_2, and then the brains were collected for
826 qPCR or immunohistochemistry analysis.

827 **Immunohistochemistry analysis**

Groups of female C57BL/6 mice were infected intranasally with rRABV or rRABV-EDAL. At indicated times post infection (pi), mouse brains were harvested and fixed in 4% paraformaldehyde for 2 days at 4°C. Tissues were then dehydrated in 30% sucrose in PBS for 48 h at 4°C, then embedded in paraffin and sliced into 4 μm sections. For immunohistochemistry (IHC), the sections were deparaffinized and rehydrated in xylene and ethanol. Endogenous peroxidase was quenched by incubation in 3% hydrogen peroxide, and antigen retrieval was performed in 0.01 M citrate buffer. Sections were blocked then incubated with primary anti-RABV P antibody (prepared in our lab, 1:500) or CD45 antibody (Servicebio, GB11066, 1:3000) overnight at 4°C. Sections were washed again then incubated with HRP-conjugated anti-mouse (Servicebio, G1211, without dilution) or anti-rabbit secondary antibodies (Servicebio, GB23303, 1:200). After washing, sections were incubated with diaminobenzidine (ServiceBio, G1211) for color development then photographed and analyzed using an XSP-C204 microscope (CIC).

Western blotting

N2a cells were lysed in RIPA buffer (Beyotime, P0013B) supplemented with 1x protease inhibitor cocktail (Roche). Total cell lysates were separated on 8-12% SDS-PAGE gels and transferred to PVDF membranes (Bio-Rad). Membranes were blocked with TBST with 5% (w/v) non-fat dry milk for 4 h, and probed with primary antibodies which were diluted with TBST and 5% (w/v) non-fat dry milk overnight in 4°C. The primary antibodies were against RABV N protein (prepared by our lab, 1:5000), H3K27me3 (Abclonal Technology, Wuhan, China, A2363, 1:2000), H3 (Abclonal Technology, A2348, 1:2000), EZH2 (CST, #5246, 1:2000), Flag tag (MBL, M185-3L, 1:10000), HA tag (MBL, M180-3, 1:10000), PCP4L1 (ProteinTech, 25933-1-AP, 1:2000) or GAPDH (ProteinTech, 60004-1-Ig, 1:5000). After rinsing, membranes were probed with HRP-conjugated anti-mouse (Boster, Wuan, China, BA1051) or anti-rabbit

856 secondary antibodies (Boster, BA1055, 1:6000), then developed using
857 BeyoECL Star kit (Beyotime, P0018A). Images were captured with an
858 Amersham Imager 600 (GE Healthcare) imaging system.

859 **EDAL-EZH2 interaction 3D structure modeling**

860 Murine EZH2 3D structure was predicted with SWISS-MODEL
861 (https://swissmodel.expasy.org/interactive) based on human EZH2 3D
862 structure (PDB code: 5HYN). Then amino acid sequence comparison was
863 conducted between human EZH2 and Murine EZH2, and 98.24% similarity
864 was calculated by Clustal2.1 (a multiple sequence alignment software,
865 https://www.ebi.ac.uk/Tools/msa/muscle/). And the high sequence similarity
866 ensures the authenticity of our predicted Murine EZH2 3D structure. EDAL-FD
867 3D structure model was predicted with RNAComposer (A automated RNA
868 structure 3D modeling server, http://rnacomposer.ibch.poznan.pl/). In order to
869 predict the interaction between EDAL functional domain (98-153 nt) and
870 Murine EZH2, the template-based docking method PRIME (Zheng, Kundrotas
871 et al., 2016) (If a template can be found, it is often more accurate than the free
872 docking method) was used to dock the EDAL and EZH2 monomer structures
873 at first. However, these two monomer structures could not find a suitable
874 template in the template library, so the free docking method 3dRPC (Huang,
875 Liu et al., 2013, Zheng, Hong et al., 2019) (A computational method was
876 designed for 3D RNA-protein complex structure prediction.) was then utilized
877 to dock EDAL and EZH2. Two atoms between EZH2 and EDAL with distance
878 less than 5 angstroms in the predicted complex structure are considered to
879 have interactions.

880 **RNA pull-down assay**

881 RNA was transcribed *in vitro* with T7 RNA polymerase (Roche, 10881767001)
882 and labeled with Biotin RNA Labeling Mix (Roche, 11685597910). The
883 synthesized RNA was treated with Rnase-free DNase I (Thermo, EN0521) and

884 then purified with MicroElute RNA Clean-Up Kit (OMEGA, R6247-01). The
885 RNA was heated to 95°C for 2 min, put on ice for 5 min and then put it at room
886 temperature for 20 min to form secondary structure. The RNA was then added
887 to the lysed cell containing overexpressed EZH2-1-337-flag and incubated for
888 2 h at 4°C. Then the Streptavidin M-280 beads (Thermo Fisher Scientific,
889 11205D) was added to the protein-RNA mix and incubated for 1 h at room
890 temperature. After being washed with wash buffer for three times, the samples
891 were then analyzed by Western blotting.

892 **_O_-GlcNAcylation labeling and detection**

893 The plasmid pCAGGS-EZH2-S73/S75/S725A-flag was co-tranfected with
894 pcDNA3.1, pcDNA-EDAL or pcDNA-revEDAL in N2a cells and treated with 5
895 mM NH_4Cl for 48 h. Then the cells were lysed and EZH2-S73/S75/S725A-flag
896 was pulled down by anti-flag beads (MBL, M185-10). The extracted protein
897 was labeled with Click-iT™ *O*-GlcNAc Enzymatic Labeling System (Invitrogen,
898 C33368) following with the manufacture's protocol. Then the *O*-GlcNAcylation
899 level of the labeled EZH2-S73/S75-S725A-flag was analyzed by Click-iT™
900 Protein Analysis Detection Kits (Invitrogen, C33370).

901 **Chromatin Immunoprecipitation Sequencing (ChIP-seq) library**
902 **construction and sequencing**

903 Briefly, N2a cell were transfected with pcDNA3.1 or pcDNA-EDAL for 48 h,
904 then the growth media of N2a cells was removed and cells were rinsed three
905 times with cold PBS. Then cells were added with formaldehyde to a final
906 concentration of 1% and incubated at room temperature for 10 min. To stop the
907 cross-linking reaction, glycine was add into cells to a final concentration of
908 0.125 M. Cells were harvested into cold PBS by scraping and transfered into a
909 1.5 ml microcentrifuge tube. After centrifugation at 1000 g for 5 min at 4°C, the
910 formaldehyde crosslinked cells were collected and resuspended in 1 ml Nuclei

Lysis Buffer (50 mM Tris-HCl pH 8.0, 10 mM EDTA pH 8.0, 1 % SDS，1 mM PMSF). Chromatin was sheared to an average size of 100-500 bp by sonication, and then centrifuged (10 min, 10000 g, 4°C). 60 µl of supernatant was diluted 10-fold with 540 µl ChIP dilution buffer (1% Triton X-100, 1.2 mM EDTA, 167 mM NaCl, and 16.7 mM Tris-HCl pH 8.0), then incubated with rotation with anti-H3K27me3 (Millipore, 07-449, 10 µg) or anti- rabbit IgG (Millipore, 12-370, 10 µg) overnight at 4°C. 50 µl protein A/G Dynabeads (Pierce™, #26162) were added to each sample and incubation continued for 2 h at 4°C on a rotating platform. Beads were pelleted then washed sequentially with low salt buffer (150 mM NaCl, 20 mM Tris–HCl pH 8.0, 0.1% SDS, 0.5% Triton X-100, and 2 mM EDTA), high salt buffer (0.1% SDS, 1% Triton X-100, 2 mM EDTA, 20 mM Tris-HCl, pH 8.1, 500 mM NaCl), LiCl buffer (0.25 M LiCl, 1% sodium deoxycholate, 10 mM Tris–HCl pH 8.0, 1% NP-40 and 1 mM EDTA), then twice with TE buffer (1 mM EDTA and 10 mM Tris–HCl pH 8.0). Chromatin was eluted from the beads by two washes with 100 µl elution buffer (100 mM $NaHCO_3$, 1% SDS), the Na^+ concentration was adjusted to 300 mM with 5 M NaCl and the crosslinks were reversed by overnight incubation in a 65°C water-bath. Samples were then incubated with 0.1 mg/ml RNase A for 1 h at 37°C, then with 1 mg/ml proteinase K for 2 h at 55°C. DNA was purified by phenol extraction and ethanol precipitation. For high-throughput sequencing, the libraries were prepared following the manufacturer's instructions (ThruPLEX DNA-seq 48S Kit, R400427) and analyzed using an Illumina NextSeq-500 system for 150 nt pair-end sequencing (ABlife Inc., Wuhan, China).

ChIP-seq data analysis

Adaptors and low quality bases were trimmed from raw sequencing reads using Cutadapt (Martin, 2011) . Reads were aligned to the mouse-GRCm38 genome using Bowtie2 (Langmead & Salzberg, 2012). To evaluate the quality

of ChIP-seq data, we performed a cross-correlation analysis, as well as FRiP and IDR analyses for the ChIP-seq data, according to the ChIP-seq guidelines provided by the ENCODE and modENCODE consortia (Kheradpour & Kellis, 2012) . Peaks enriched by immunoprecipitation (compared to input DNA) were identified using MACS v1.4 (Zhang, Liu et al., 2008) . We selected peaks with *p-values* less than 10^{-5}. All peaks from each sample were clustered by BEDTools (Quinlan & Hall, 2010). In this step, peaks with at least 1 bp overlap or book-ended features are merged. To associate peaks with genes, we set 10000 bp as the upstream limit for the distance from the peak maximum to the TSS (transcript start site), and 3000 bp as the downstream limit for distance from the peak maximum to the TSS.

ChIP-qPCR

Formaldehyde crosslinking of N2a cells, chromatin sonication and immunoprecipitation were performed following the same procedures as the ChIP-seq section described above. The DNA pellet was suspended in 10 μl DEPC-water. Real-time PCR was then performed using a QuantStudio 6 Flex System (ABI) according to the manufacturer's standard protocol. Input was used to normalize the amount of each sample as an internal control. Assays were repeated at least three times and expressed as Ct values. All PCR primer sequences can be found in Appendix Table S2.

Statistical analysis

Statistical analysis was performed using the R software (https://www.r-project.org/) or GraphPad Prism 6. Significance of differences was evaluated with either Student's t-test, when only two groups were compared, or hypergeometric test for venn diagram. Survival percent was analyzed by log rank test. Hierarchical clustering was performed by Cluster3.0 or heatmap function in R. No statistical method was used to predetermine

966 sample sizes. *P <0.05, **P <0.01 and ***P < 0.001.

967 **ACKNOWLEDGMENT**

968 This study was partially supported by the National Program on Key Research
969 Project of China (2016YFD0500400), the Fundamental Research Funds for
970 the Central Universities (2662015PY227) and the National Natural Science
971 Foundation of China (31522057). This study was also partially supported by
972 the Appreciate the Beauty of Life Incorporation (ABL2014-09030).

973 **Author contributions**

974 Conceived and designed the experiments: LZ YZ BKS. Performed the
975 experiments: BKS DC WL QW BT JH YYL SYL JX HJ ZCL LL FH RML.
976 Analyzed the data: BKS DC MC MZ HCC ZFF YZ LZ. Wrote the paper: BKS
977 DC YZ LZ.

978 **Data availability**

979 RNA-seq and ChIP-seq data reported in this study are deposited in Gene
980 Expression Omnibus (GEO) with accession number GSE107310
981 (https://www.ncbi.nlm.nih.gov/geo/query/acc.cgi?acc=GSE107310). The data
982 which support the findings of this study are available from the corresponding
983 author on reasonable request.

984 **Competing interests**

985 The authors declare no competing financial interests.

986 **Supplementary information**

987 Supplementary information includes 2 appendix figures and 2 appendix tables.

988

989

REFERENCES

2Nd SP, Mcgavern DB (2015) Viral diseases of the central nervous system. Current Opinion in Virology 11: 44-54

Arbuckle JH, Gardina PJ, Gordon DN, Hickman HD, Yewdell JW, Pierson TC, Myers TG, Kristie TM (2017) Inhibitors of the Histone Methyltransferases EZH2/1 Induce a Potent Antiviral State and Suppress Infection by Diverse Viral Pathogens. Mbio 8: e01141-17

Batista PJ, Chang HY (2013) Long noncoding RNAs: cellular address codes in development and disease. Cell 152: 1298-307

Bonasio R, Shiekhattar R (2014) Regulation of Transcription by Long Noncoding RNAs. Annual Review of Genetics 48: 433

Bradshaw MJ, Venkatesan A (2016) Herpes Simplex Virus-1 Encephalitis in Adults: Pathophysiology, Diagnosis, and Management. Neurotherapeutics : the journal of the American Society for Experimental NeuroTherapeutics 13: 493-508

Briggs J, Wolvetang E, Mattick J, Rinn J, Barry G (2015) Mechanisms of Long Non-coding RNAs in Mammalian Nervous System Development, Plasticity, Disease, and Evolution. Neuron 88: 861

Buchmann RC, Asad S, Wolf JN, Mohannath G, Bisaro DM (2009) Geminivirus AL2 and L2 proteins suppress transcriptional gene silencing and cause genome-wide reductions in cytosine methylation. J Virol 83: 5005-13

Bulfone A, Caccioppoli C, Pardini C, Faedo A, Martinez S, Martinez S, Banfi S (2004) Pcp4l1, a novel gene encoding a Pcp4-like polypeptide, is expressed in specific domains of the developing brain. Gene Expression Patterns 4: 297-301

Carod-Artal FJ (2016) Epidemiology and neurological complications of infection by the Zika virus: a new emerging neurotropic virus. Revista de neurologia 62: 317-28

Carpenter S, Fitzgerald KA (2018) Cytokines and Long Noncoding RNAs. Cold Spring Harbor perspectives in biology 10

Chu CS, Lo PW, Yeh YH, Hsu PH, Peng SH, Teng YC, Kang ML, Wong CH, Juan LJ (2014) O-GlcNAcylation regulates EZH2 protein stability and function. Proceedings of the National Academy of Sciences of the United States of America 111: 1355-60

Conway E, Healy E, Bracken AP (2015) PRC2 mediated H3K27 methylations in cellular identity and cancer. Current Opinion in Cell Biology 37: 42-48

Davidovich C, Cech TR (2015) The recruitment of chromatin modifiers by long noncoding RNAs: lessons from PRC2. RNA (New York, NY) 21: 2007-22

Davidovich C, Wang X, Cifuentes-Rojas C, Goodrich KJ, Gooding AR, Lee JT, Cech TR (2015a) Toward a consensus on the binding specificity and promiscuity of PRC2 for RNA. Mol Cell 57: 552-8

Davidovich C, Wang X, CifuentesRojas C, Goodrich KJ, Gooding AR, Lee JT, Cech TR (2015b) Towards a Consensus on the Binding Specificity and Promiscuity of PRC2 for RNA. Molecular Cell 57: 552-558

Davidovich C, Zheng L, Goodrich KJ, Cech TR (2013) Promiscuous RNA binding by Polycomb repressive complex 2. Nature structural & molecular biology 20: 1250-7

Fang S, Zhang L, Guo J, Niu Y, Wu Y, Li H, Zhao L, Li X, Teng X, Sun X (2017) NONCODEV5: a comprehensive annotation database for long non-coding RNAs. Nucleic Acids Research 46

Fatica A, Bozzoni I (2014) Long non-coding RNAs: new players in cell differentiation and development. Nature Reviews Genetics 15: 7-21

1033 Fisher CR, Schnell MJ (2018) New developments in rabies vaccination. Revue scientifique et
1034 technique (International Office of Epizootics) 37: 657-672
1035 Fortes P, Morris KV (2016) Long noncoding RNAs in viral infections. Virus research 212: 1-11
1036 Fragkoudis R, Dixon-Ballany CM, Zagrajek AK, Kedzierski L, Fazakerley JK (2018) Following Acute
1037 Encephalitis, Semliki Forest Virus is Undetectable in the Brain by Infectivity Assays but Functional
1038 Virus RNA Capable of Generating Infectious Virus Persists for Life. Viruses 10
1039 Gagnidze K, Hajdarovic KH, Moskalenko M, Karatsoreos IN, McEwen BS, Bulloch K (2016) Nuclear
1040 receptor REV-ERBalpha mediates circadian sensitivity to mortality in murine vesicular stomatitis
1041 virus-induced encephalitis. Proceedings of the National Academy of Sciences of the United States of
1042 America 113: 5730-5
1043 Hanover JA, Krause MW, Love DC (2012) Bittersweet memories: linking metabolism to epigenetics
1044 through O-GlcNAcylation. Nature reviews Molecular cell biology 13: 312-21
1045 Hart GW, Slawson C, Ramirez-Correa G, Lagerlof O (2011) Cross talk between O-GlcNAcylation and
1046 phosphorylation: roles in signaling, transcription, and chronic disease. Annual review of biochemistry
1047 80: 825-58
1048 Huang Y, Li H, Xiao Y (2016) Using 3dRPC for RNA-protein complex structure prediction. Biophysics
1049 reports 2: 95-99
1050 Huang Y, Li H, Xiao Y (2018) 3dRPC: a web server for 3D RNA-protein structure prediction.
1051 Bioinformatics 34: 1238-1240
1052 Huang Y, Liu S, Guo D, Li L, Xiao Y (2013) A novel protocol for three-dimensional structure
1053 prediction of RNA-protein complexes. Scientific reports 3: 1887
1054 Imamura K, Imamachi N, Akizuki G, Kumakura M, Kawaguchi A, Nagata K, Kato A, Kawaguchi Y,
1055 Sato H, Yoneda M (2014) Long Noncoding RNA NEAT1-Dependent SFPQ Relocation from Promoter
1056 Region to Paraspeckle Mediates IL8 Expression upon Immune Stimuli. Molecular Cell 53: 393-406
1057 Jadhav U, Nalapareddy K, Saxena M, O'Neill NK, Pinello L, Yuan GC, Orkin SH, Shivdasani RA
1058 (2016) Acquired tissue-specific promoter bivalency is a basis for PRC2 necessity in adult cells. Cell
1059 165: 1389-1400
1060 Jiang M, Zhang S, Yang Z, Lin H, Zhu J, Liu L, Wang W, Liu S, Liu W, Ma Y, Zhang L, Cao X (2018)
1061 Self-Recognition of an Inducible Host lncRNA by RIG-I Feedback Restricts Innate Immune Response.
1062 Cell 173: 906-919.e13
1063 Jin JJ, Lv W, Xia P, Xu ZY, Zheng AD, Wang XJ, Wang SS, Zeng R, Luo HM, Li GL, Zuo B (2018)
1064 Long noncoding RNA SYISL regulates myogenesis by interacting with polycomb repressive complex 2.
1065 Proceedings of the National Academy of Sciences of the United States of America 115: E9802-e9811
1066 Jin X, Xu XE, Jiang YZ, Liu YR, Sun W, Guo YJ, Ren YX, Zuo WJ, Hu X, Huang SL, Shen HJ, Lan F,
1067 He YF, Hu GH, Di GH, He XH, Li DQ, Liu S, Yu KD, Shao ZM (2019) The endogenous
1068 retrovirus-derived long noncoding RNA TROJAN promotes triple-negative breast cancer progression
1069 via ZMYND8 degradation. Science advances 5: eaat9820
1070 Johnsson P, Lipovich L, Grander D, Morris KV (2014) Evolutionary conservation of long non-coding
1071 RNAs; sequence, structure, function. Biochimica et biophysica acta 1840: 1063-71
1072 Justin N, Zhang Y, Tarricone C, Martin SR, Chen S, Underwood E, De Marco V, Haire LF, Walker PA,
1073 Reinberg D, Wilson JR, Gamblin SJ (2016) Structural basis of oncogenic histone H3K27M inhibition
1074 of human polycomb repressive complex 2. Nature communications 7: 11316
1075 Kambara H, Niazi F, Kostadinova L, Moonka DK, Siegel CT, Post AB, Carnero E, Barriocanal M,

1076 Fortes P, Anthony DD (2014) Negative regulation of the interferon response by an interferon-induced
1077 long non-coding RNA. Nucleic Acids Research 42: 10668-80
1078 Kaneko S, Li G, Son J, Xu CF, Margueron R, Neubert TA, Reinberg D (2010) Phosphorylation of the
1079 PRC2 component Ezh2 is cell cycle-regulated and up-regulates its binding to ncRNA. Genes &
1080 development 24: 2615-20
1081 Kasinath V, Faini M, Poepsel S, Reif D, Feng XA, Stjepanovic G, Aebersold R, Nogales E (2018)
1082 Structures of human PRC2 with its cofactors AEBP2 and JARID2. Science (New York, NY) 359:
1083 940-944
1084 Kheradpour P, Kellis M (2012) ChIP-seq guidelines and practices of the ENCODE and modENCODE
1085 consortia. Genome Research 22: 1813
1086 Kim D, Pertea G, Trapnell C, Pimentel H, Kelley R, Salzberg SL (2013) TopHat2: accurate alignment
1087 of transcriptomes in the presence of insertions, deletions and gene fusions. Genome Biology 14: R36
1088 Kim KH, Roberts CWM (2016) Targeting EZH2 in cancer. Nature Medicine 22: 128-134
1089 Knipe DM, Raja P, Lee J (2017) Viral gene products actively promote latent infection by epigenetic
1090 silencing mechanisms. Curr Opin Virol 23: 68-74
1091 Kong L, Zhang Y, Ye ZQ, Liu XQ, Zhao SQ, Wei L, Gao G (2007) CPC: assess the protein-coding
1092 potential of transcripts using sequence features and support vector machine. Nucleic Acids Research 35:
1093 W345
1094 Kramer JM, Kochinke K, Oortveld MA, Marks H, Kramer D, de Jong EK, Asztalos Z, Westwood JT,
1095 Stunnenberg HG, Sokolowski MB, Keleman K, Zhou H, van Bokhoven H, Schenck A (2011)
1096 Epigenetic regulation of learning and memory by Drosophila EHMT/G9a. PLoS biology 9: e1000569
1097 Langmead B, Salzberg SL (2012) Fast gapped-read alignment with Bowtie 2. Nature methods 9: 357
1098 Lee CH, Yu JR, Kumar S, Jin Y, LeRoy G, Bhanu N, Kaneko S, Garcia BA, Hamilton AD, Reinberg D
1099 (2018) Allosteric Activation Dictates PRC2 Activity Independent of Its Recruitment to Chromatin. Mol
1100 Cell 70: 422-434.e6
1101 Lee JT (2012) Epigenetic regulation by long noncoding RNAs. Science (New York, NY) 338: 1435-9
1102 Lewis BA, Hanover JA (2014) O-GlcNAc and the epigenetic regulation of gene expression. The
1103 Journal of biological chemistry 289: 34440-8
1104 Li J, Witten DM, Johnstone IM, Tibshirani R (2012) Normalization, testing, and false discovery rate
1105 estimation for RNA-sequencing data. Biostatistics 13: 523-38
1106 Li Z, Hou P, Fan D, Dong M, Ma M, Li H, Yao R, Li Y, Wang G, Geng P, Mihretab A, Liu D, Zhang Y,
1107 Huang B, Lu J (2017) The degradation of EZH2 mediated by lncRNA ANCR attenuated the invasion
1108 and metastasis of breast cancer. Cell death and differentiation 24: 59-71
1109 Lieberman PM (2016) Epigenetics and Genetics of Viral Latency. Cell Host Microbe 19: 619-28
1110 Lin H, Jiang M, Liu L, Yang Z, Ma Z, Liu S, Ma Y, Zhang L, Cao X (2019) The long noncoding RNA
1111 Lnczc3h7a promotes a TRIM25-mediated RIG-I antiviral innate immune response. Nature
1112 immunology 20: 812-823
1113 Lin MF, Jungreis I, Kellis M (2011) PhyloCSF: a comparative genomics method to distinguish
1114 protein-coding and non-coding regions. Bioinformatics 27: i275-i282
1115 Liu S, Wang Z, Chen D, Zhang B, Tian R, Wu J, Zhang Y, Xu K, Yang L, Cheng C (2017) Annotation
1116 and cluster analysis of spatiotemporal- and sex-related lncRNA expression in Rhesus macaque brain.
1117 Genome Research 27: 1608
1118 Lo PW, Shie JJ, Chen CH, Wu CY, Hsu TL, Wong CH (2018) O-GlcNAcylation regulates the stability

and enzymatic activity of the histone methyltransferase EZH2. Proceedings of the National Academy of Sciences of the United States of America 115: 7302-7307

Ludlow M, Kortekaas J, Herden C, Hoffmann B, Tappe D, Trebst C, Griffin DE, Brindle HE, Solomon T, Brown AS, van Riel D, Wolthers KC, Pajkrt D, Wohlsein P, Martina BEE, Baumgartner W, Verjans GM, Osterhaus A (2016) Neurotropic virus infections as the cause of immediate and delayed neuropathology. Acta Neuropathol 131: 159-184

Ma H, Han P, Ye W, Chen H, Zheng X, Cheng L, Zhang L, Yu L, Wu XA, Xu Z (2017) The Long Noncoding RNA NEAT1 Exerts Antihantaviral Effects by Acting as Positive Feedback for RIG-I Signaling. Journal of Virology 91: JVI.02250-16

Manglani M, McGavern DB (2018) New advances in CNS immunity against viral infection. Curr Opin Virol 28: 116-126

Margueron R, Reinberg D (2011) The Polycomb complex PRC2 and its mark in life. Nature 469: 343

Martin M (2011) Cutadapt removes adapter sequences from high-throughput sequencing reads. Embnet Journal 17

Mccabe MT, Ott HM, Ganji G, Korenchuk S, Thompson C, Van Aller GS, Liu Y, Graves AP, Rd DPA, Diaz E (2012) EZH2 inhibition as a therapeutic strategy for lymphoma with EZH2-activating mutations. Nature 492: 108-12

Mercer TR, Dinger ME, Mattick JS (2009) Long non-coding RNAs: insights into functions. Nature Reviews Genetics 10: 155-159

Mercer TR, Mattick JS (2013) Structure and function of long noncoding RNAs in epigenetic regulation. Nature structural & molecular biology 20: 300-307

Merkling SH, Bronkhorst AW, Kramer JM, Overheul GJ, Schenck A, Van Rij RP (2015) The epigenetic regulator G9a mediates tolerance to RNA virus infection in Drosophila. PLoS pathogens 11: e1004692

Meyding-Lamade U, Craemer EM (2018) [Winners of globalization: dengue viruses and Japanese encephalitis virus-Diseases in neurology]. Der Nervenarzt 89: 1338-1343

Morgan MAJ, Morgan JI (2012) Pcp4l1 contains an auto-inhibitory element that prevents its IQ motif from binding to calmodulin. Journal of Neurochemistry 121: 843-51

Mudge JM, Harrow J (2015) Creating reference gene annotation for the mouse C57BL6/J genome assembly. Mammalian Genome 26: 366-378

N B (2013) Noncoding RNA and Polycomb recruitment. RNA (New York,NY) 19: 429-442

Olival KJ, Daszak P (2005) The ecology of emerging neurotropic viruses. J Neurovirol 11: 441-6

Ouyang J, Hu J, Chen JL (2016) lncRNAs regulate the innate immune response to viral infection. Wiley interdisciplinary reviews RNA 7: 129-43

Ouyang J, Zhu X, Chen Y, Wei H, Chen Q, Chi X, Qi B, Zhang L, Zhao Y, Gao GF (2014) NRAV, a long noncoding RNA, modulates antiviral responses through suppression of interferon-stimulated gene transcription. Cell Host & Microbe 16: 616

Qin H, Xu J, Gong L, Jiang B, Zhao W (2019) The long noncoding RNA ST7-AS1 promotes laryngeal squamous cell carcinoma by stabilizing CARM1. Biochemical and biophysical research communications 512: 34-40

Quek XC, Thomson DW, Maag JL, Bartonicek N, Signal B, Clark MB, Gloss BS, Dinger ME (2015) lncRNAdb v2.0: expanding the reference database for functional long noncoding RNAs. Nucleic Acids Research 43: 168-73

Quinlan AR, Hall IM (2010) Quinlan AR, Hall IM. BEDTools: a flexible suite of utilities for

1162 comparing genomic features. Bioinformatics 26: 841-842
1163 Ringrose L (2017) Noncoding RNAs in Polycomb and Trithorax Regulation: A Quantitative
1164 Perspective. Annual Review of Genetics 51
1165 Rinn JL, Kertesz M, Wang JK, Squazzo SL, Xu X, Brugmann SA, Goodnough LH, Helms JA,
1166 Farnham PJ, Segal E, Chang HY (2007) Functional demarcation of active and silent chromatin domains
1167 in human HOX loci by noncoding RNAs. Cell 129: 1311-23
1168 Rivas E, Clements J, Eddy SR (2017) A statistical test for conserved RNA structure shows lack of
1169 evidence for structure in lncRNAs. Nature methods 14: 45-48
1170 Robinson MD, Oshlack A (2010) A scaling normalization method for differential expression analysis of
1171 RNA-seq data. Genome Biology 11: 1-9
1172 Romanel E, Silva TF, Correa RL, Farinelli L, Hawkins JS, Schrago CE, Vaslin MF (2012) Global
1173 alteration of microRNAs and transposon-derived small RNAs in cotton (Gossypium hirsutum) during
1174 Cotton leafroll dwarf polerovirus (CLRDV) infection. Plant molecular biology 80: 443-60
1175 Ruiz-Ferrer V, Voinnet O (2009) Roles of plant small RNAs in biotic stress responses. Annual review
1176 of plant biology 60: 485-510
1177 Schnell MJ, McGettigan JP, Wirblich C, Papaneri A (2010) The cell biology of rabies virus: using
1178 stealth to reach the brain. Nature reviews Microbiology 8: 51-61
1179 Scott RS (2017) Epstein-Barr virus: a master epigenetic manipulator. Curr Opin Virol 26: 74-80
1180 Simon JA, Kingston RE (2009) Mechanisms of polycomb gene silencing: knowns and unknowns.
1181 Nature reviews Molecular cell biology 10: 697-708
1182 Sun W, Yang Y, Xu C, Guo J (2017) Regulatory mechanisms of long noncoding RNAs on gene
1183 expression in cancers. Cancer Genet 216-217: 105-110
1184 Tian D, Luo Z, Zhou M, Li M, Yu L, Wang C, Yuan J, Li F, Tian B, Sui B, Chen H, Fu ZF, Zhao L
1185 (2016) Critical Role of K1685 and K1829 in the Large Protein of Rabies Virus in Viral Pathogenicity
1186 and Immune Evasion. J Virol 90: 232-44
1187 Trapnell C, Roberts A, Goff L, Pertea G, Kim D, Kelley DR, Pimentel H, Salzberg SL, Rinn JL,
1188 Pachter L (2012) Differential gene and transcript expression analysis of RNA-seq experiments with
1189 TopHat and Cufflinks. Nature Protocols 7: 562
1190 Volders PJ, Verheggen K, Menschaert G, Vandepoele K, Martens L, Vandesompele J, Mestdagh P
1191 (2015) An update on LNCipedia: a database for annotated human lncRNA sequences. Nucleic Acids
1192 Research 43: 174-80
1193 Wan J, Zhan J, Li S, Ma J, Xu W, Liu C, Xue X, Xie Y, Fang W, Chin YE, Zhang H (2015)
1194 PCAF-primed EZH2 acetylation regulates its stability and promotes lung adenocarcinoma progression.
1195 Nucleic Acids Res 43: 3591-604
1196 Wang J, Cheng P, Pavlyukov MS, Yu H, Zhang Z, Kim SH, Minata M, Mohyeldin A, Xie W, Chen D,
1197 Goidts V, Frett B, Hu W, Li H, Shin YJ, Lee Y, Nam DH, Kornblum HI, Wang M, Nakano I (2017)
1198 Targeting NEK2 attenuates glioblastoma growth and radioresistance by destabilizing histone
1199 methyltransferase EZH2. The Journal of clinical investigation 127: 3075-3089
1200 Wang KC, Chang HY (2011) Molecular mechanisms of long noncoding RNAs. Molecular Cell 43: 904
1201 Wang P, Xue Y, Han Y, Lin L, Wu C, Xu S, Jiang Z, Xu J, Liu Q, Cao X (2014) The STAT3-binding
1202 long noncoding RNA lnc-DC controls human dendritic cell differentiation. Science (New York, NY)
1203 344: 310-3
1204 Wang X, Goodrich KJ, Gooding AR, Naeem H, Archer S, Paucek RD, Youmans DT, Cech TR,

Davidovich C (2017) Targeting of Polycomb Repressive Complex 2 to RNA by Short Repeats of Consecutive Guanines. Molecular Cell 65: 1056-1067

Wu SC, Zhang Y (2011) Cyclin-dependent kinase 1 (CDK1)-mediated phosphorylation of enhancer of zeste 2 (Ezh2) regulates its stability. The Journal of biological chemistry 286: 28511-9

Yang LP, Fang YY, An CP, Dong L, Zhang ZH, Chen H, Xie Q, Guo HS (2013) C2-mediated decrease in DNA methylation, accumulation of siRNAs, and increase in expression for genes involved in defense pathways in plants infected with beet severe curly top virus. The Plant journal : for cell and molecular biology 73: 910-7

Zhang Y, Liu T, Meyer CA, Eeckhoute J, Johnson DS, Bernstein BE, Nusbaum C, Myers RM, Brown M, Li W (2008) Model-based analysis of ChIP-Seq (MACS). Genome Biology 9: R137

Zhang Z, Chen H, Huang X, Xia R, Zhao Q, Lai J, Teng K, Li Y, Liang L, Du Q, Zhou X, Guo H, Xie Q (2011) BSCTV C2 attenuates the degradation of SAMDC1 to suppress DNA methylation-mediated gene silencing in Arabidopsis. The Plant cell 23: 273-88

Zheng J, Hong X, Xie J, Tong X, Liu S (2019) P3DOCK: a protein-RNA docking webserver based on template-based and template-free docking. Bioinformatics

Zheng J, Kundrotas PJ, Vakser IA, Liu S (2016) Template-Based Modeling of Protein-RNA Interactions. PLoS computational biology 12: e1005120

FIGURES

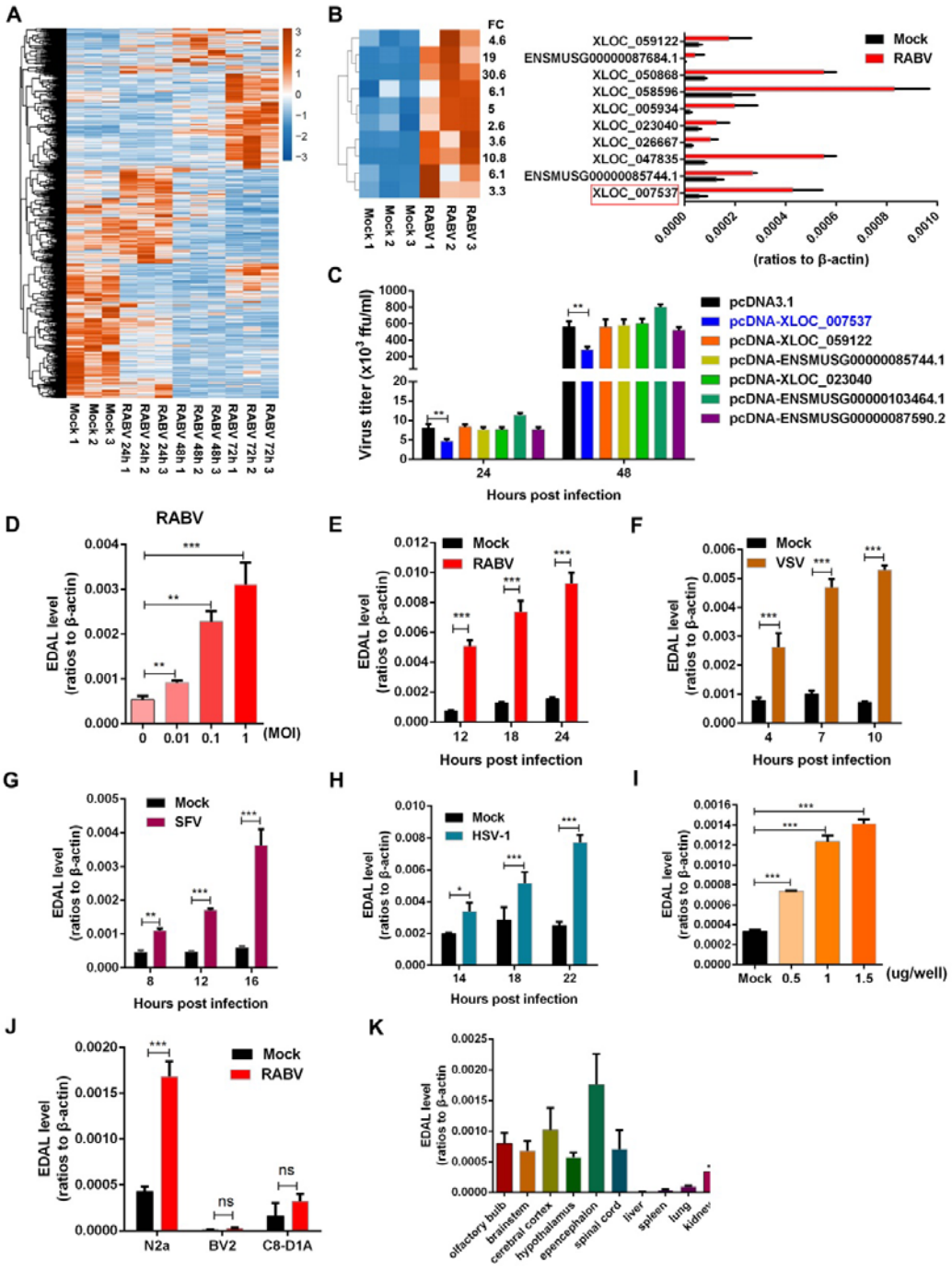

Figure 1. LncRNA EDAL is up-regulated after viral infection.

A. Total 1434 differentially expressed lncRNAs was identified by RNA-seq analysis in RABV-infected N2a cells compared with mock-infected cells (*n*=3; 2

fold change (FC) and 0.01 *p-value*). These lncRNAs were clustered and shown by heatmap.

B. Ten of the differentially expressed lncRNAs were selected and clustered in a heatmap (left), the corresponding express level were confirmed by qPCR (right).

C. The indicated up-regulated lncRNAs were selected and expressed in N2a cells. At 12 h post transfection, the cells were infected with RABV at MOI 0.01 and virus titers in supernatants were measured at indicated time point.

D. N2a cells were infected with RABV at different MOIs for 24 h and EDAL level was analyzed by qPCR.

E,F,G,H. N2a cells were infected with RABV (**E**), VSV (**F**), SFV (**G**) or HSV-1 (**H**) at MOI 1 and at indicated time points post infection. EDAL level were determined by qPCR.

I. N2a cells were transfected with RABV genomic RNA at different doses for 24 h and EDAL level was analyzed by qPCR.

J. The basal or induced level of EDAL (infected with RABV at MOI 1 for 24 h) in different cell lines were determined by qPCR.

K. The basal level of EDAL in different tissues was analyzed by qPCR.

Statistical analysis of grouped comparisons was carried out by student's t test(*$P < 0.05$; **P<0.01; ***P<0.001). Bar graph represents means ± SD, $n = 3$.

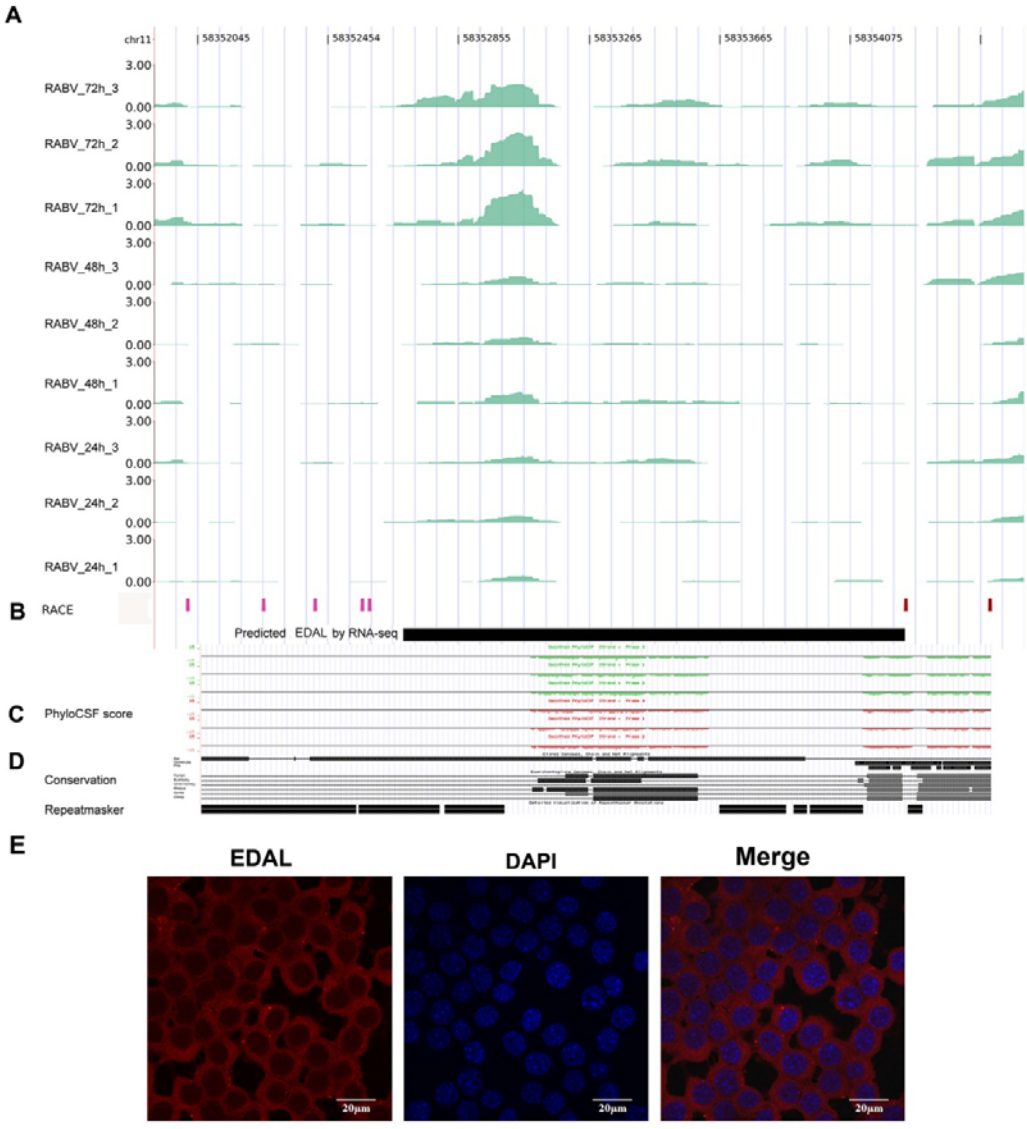

1261

1262 **Figure EV1. EDAL transcriptome analysis. (Related to Figure 1)**

1263 **A.** Read density of EDAL. The read density is based on normalized RNA-seq
1264 signals (TPM) for each sample after RABV infection. The nine tracks show
1265 RNA-seq read density at three time points after RABV infection, with three
1266 replicates per time point. Density is shown on the y-axis.

1267 **B.** The RACE track shows the genomic location of RNA ends detected by 5'
1268 RACE (pink) and 3' RACE (red). The black rectangle indicates the predicted
1269 genomic location of EDAL.

C. The PhyloCSF score track shows protein-coding scores calculated by PhyloCSF. Scores below zero indicate non-coding features. The repeated masker track shows predicted repeat sequences.

D. Conserved and repeated sequences in EDAL. Sequence analyses were performed using the UCSC genome browser.

E. RNA fluorescent *in situ* hybridization (FISH) assay were performed in N2a cell. Red-EDAL, Blue-4', 6-Diamidino-2-phenylindole dihydrochloride (DAPI). Scale bar, 20 μm.

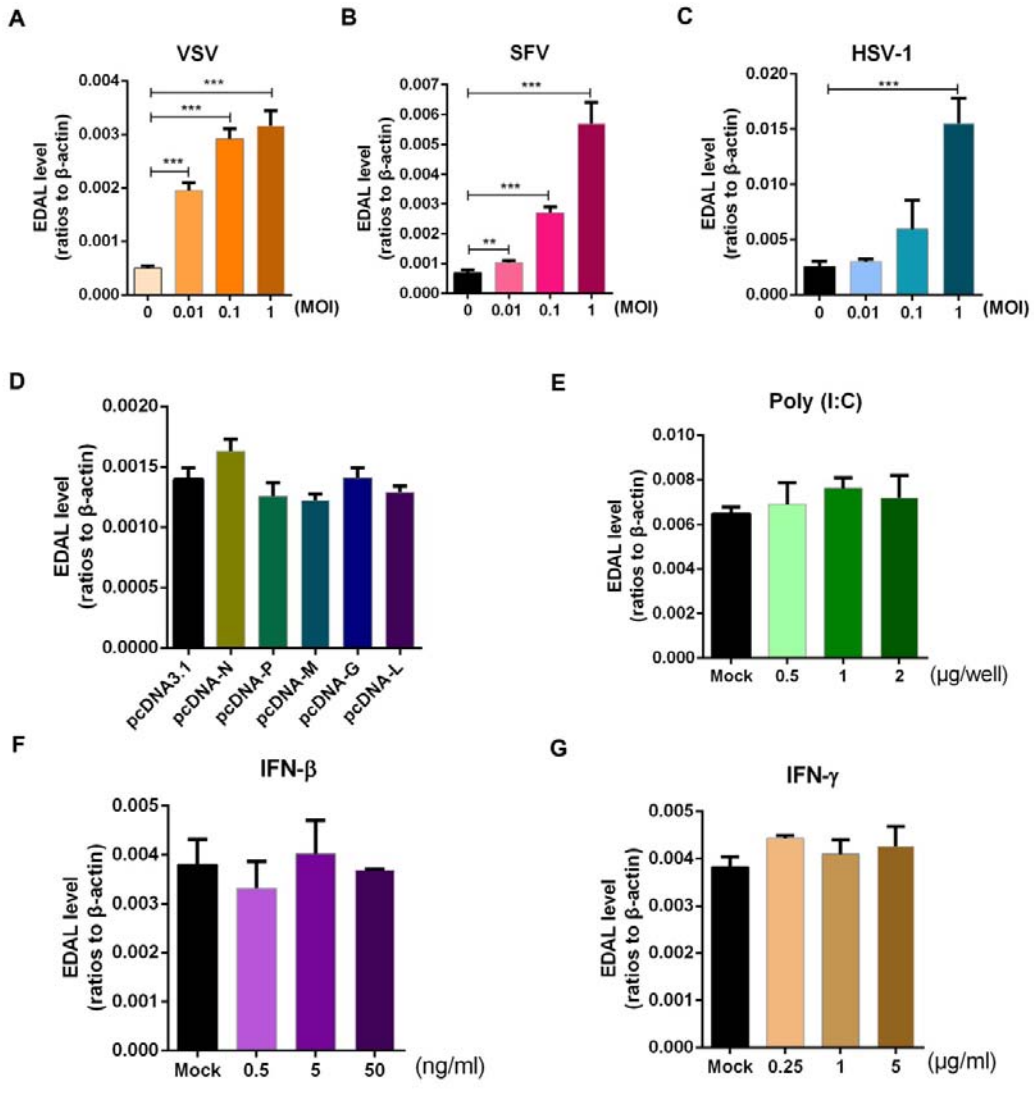

Figure EV2. EDAL is not up-regulated by RABV proteins, dsRNA, or interferons. (Related to Figure 1)

A. N2a cells were infected with VSV at different MOIs for 12 h and EDAL level was analyzed by qPCR.

B. N2a cells were infected with SFV at different MOIs for 18 h and EDAL level was analyzed by qPCR.

C. N2a cells were infected with HSV-1 at different MOIs for 18 h and EDAL level was analyzed by qPCR.

D. N2a cells were transfected with plasmids expressing different RABV proteins. EDAL levels were analyzed by qPCR at 24 h post transfection.

E. N2a cells were transfected with poly(I:C) (a mimic of dsRNA) at indicated doses. EDAL levels were measured by qPCR at 24 h post transfection.

F,G N2a cells were treated with IFN-β (**F**) or IFN-γ (**G**) for 24 h. EDAL levels were analyzed by qPCR.

Statistical analysis of grouped comparisons was carried out by student's t test(**P<0.01; ***P<0.001). Bar graph represents means ± SD, *n* = 3.

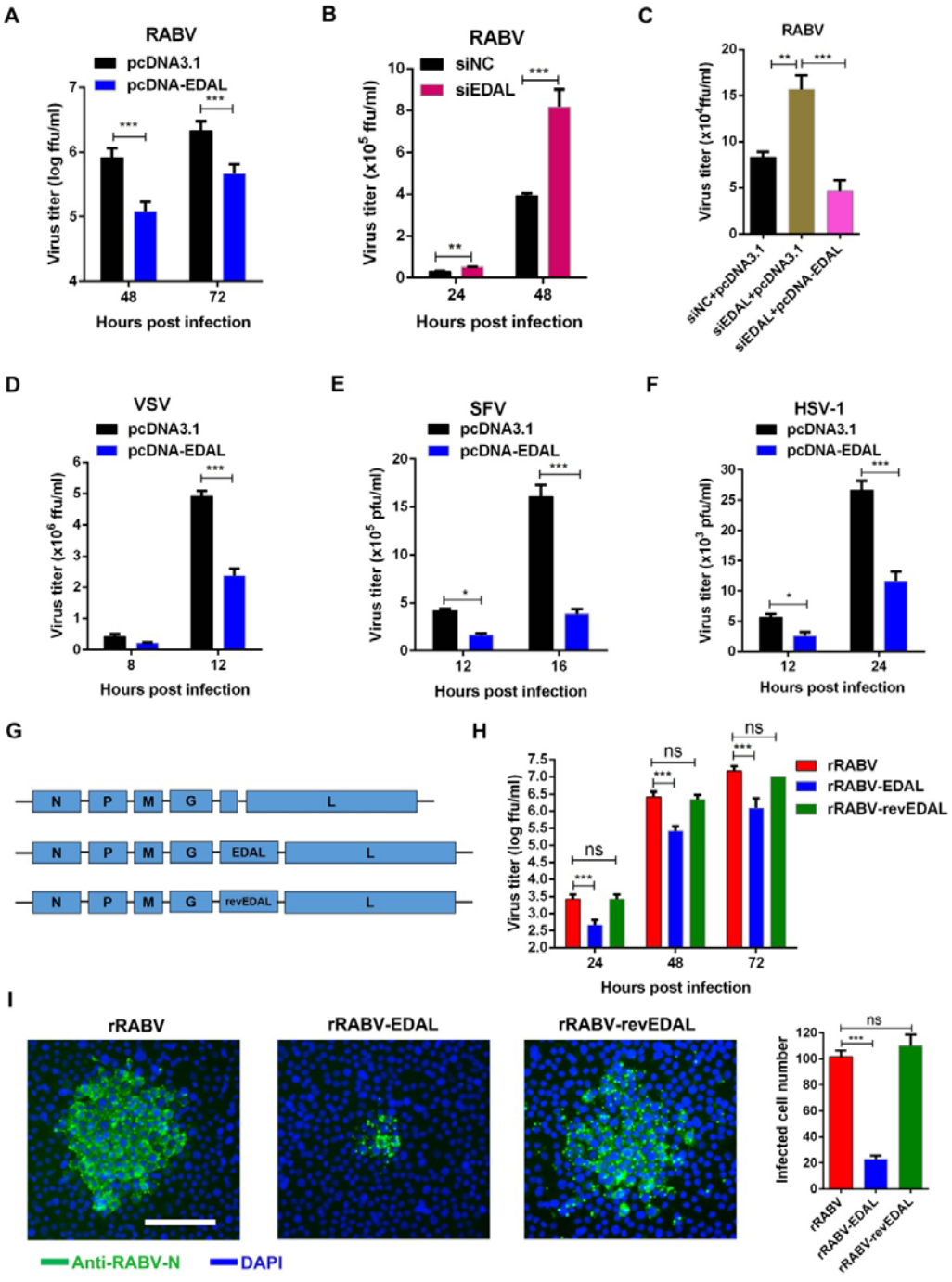

Figure 2. EDAL inhibits viral replication in neuronal cells.

A. N2a cells were transfected with pcDNA3.1 or pcDNA-EDAL, then at 12 h post transfection the cells were infected with RABV at MOI 0.01 and virus titers were measured at indicated time points.

B. N2a cells were transfected with EDAL specific siRNA (siEDAL) and at 12 h post transfection, the cells were infected with RABV at MOI 0.01 and virus titers were measured at indicated time points.

C. N2a cells were transfected with siEDAL or siNC (negative control) for 8 h and then transfected with pcDNA3.1 or pcDNA-EDAL. At 12 h post transfection, the cells were infected with RABV at MOI 0.01 for 24 h and virus titers in the cell supernatant were measured.

D. N2a cells were transfected with pcDNA3.1 or pcDNA-EDAL, then at 12 h post transfection the cells were infected with VSV at MOI 0.01 and virus titers were measured at indicated time points.

E. N2a cells were transfected with pcDNA3.1 or pcDNA-EDAL, then at 24 h post transfection the cells were infected with SFV at MOI 0.01 and virus titers were measured at indicated time points.

F. N2a cells were transfected with pcDNA3.1 or pcDNA-EDAL, then at 12 h post transfection the cells were infected with HSV-1 at MOI 0.01 and virus titers were measured at indicated time points.

G,H. EDAL and reverse EDAL (revEDAL) were inserted into the genome of a recombinant RABV (rRABV), named rRABV-EDAL and rRABV-revEDAL respectively (**G**), and their growth kinetics in N2a cells (MOI=0.01) were compared (**H**).

I. N2a cells were infected with rRABV, rRABV-EDAL or rRABV-revEDAL at MOI 0.005 for 48 h and the viral spread were compared by calculating the cell numbers within the fluorescence focus. Scale bar, 50 μm.

Statistical analysis of grouped comparisons was carried out by student's t test(*P < 0.05;**P<0.01; ***P<0.001). Bar graph represents means ± SD, n = 3.

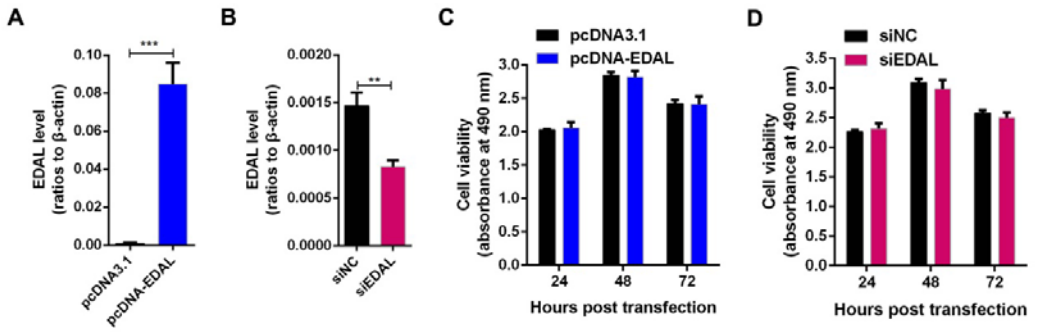

Figure EV3. Cell viability post overexpressing or silencing EDAL. (Related to Figure 2)

A. EDAL was cloned into a mammalian expression vector pcDNA3.1, named pcDNA-EDAL. After transfection in N2a cells, the expression level of EDAL was measured by qPCR.

B.N2a cells were transfected with EDAL specific siRNA (siEDAL) or siNC then the level of EDAL was confirmed by qPCR.

C. N2a cells were transfected with pcDNA3.1 or pcDNA-EDAL for indicated times, cell viability was evaluated using a Cell Titer 96 AQueous One Solution cell proliferation assay kits (G3582) from Promega.

D. N2a cells were transfected with siEDAL or siNC for indicated times, cell viability was measured.

Statistical analysis of grouped comparisons was carried out by student's t test(*P < 0.05; **P<0.01; ***P<0.001). Bar graph represents means ± SD, n = 3.

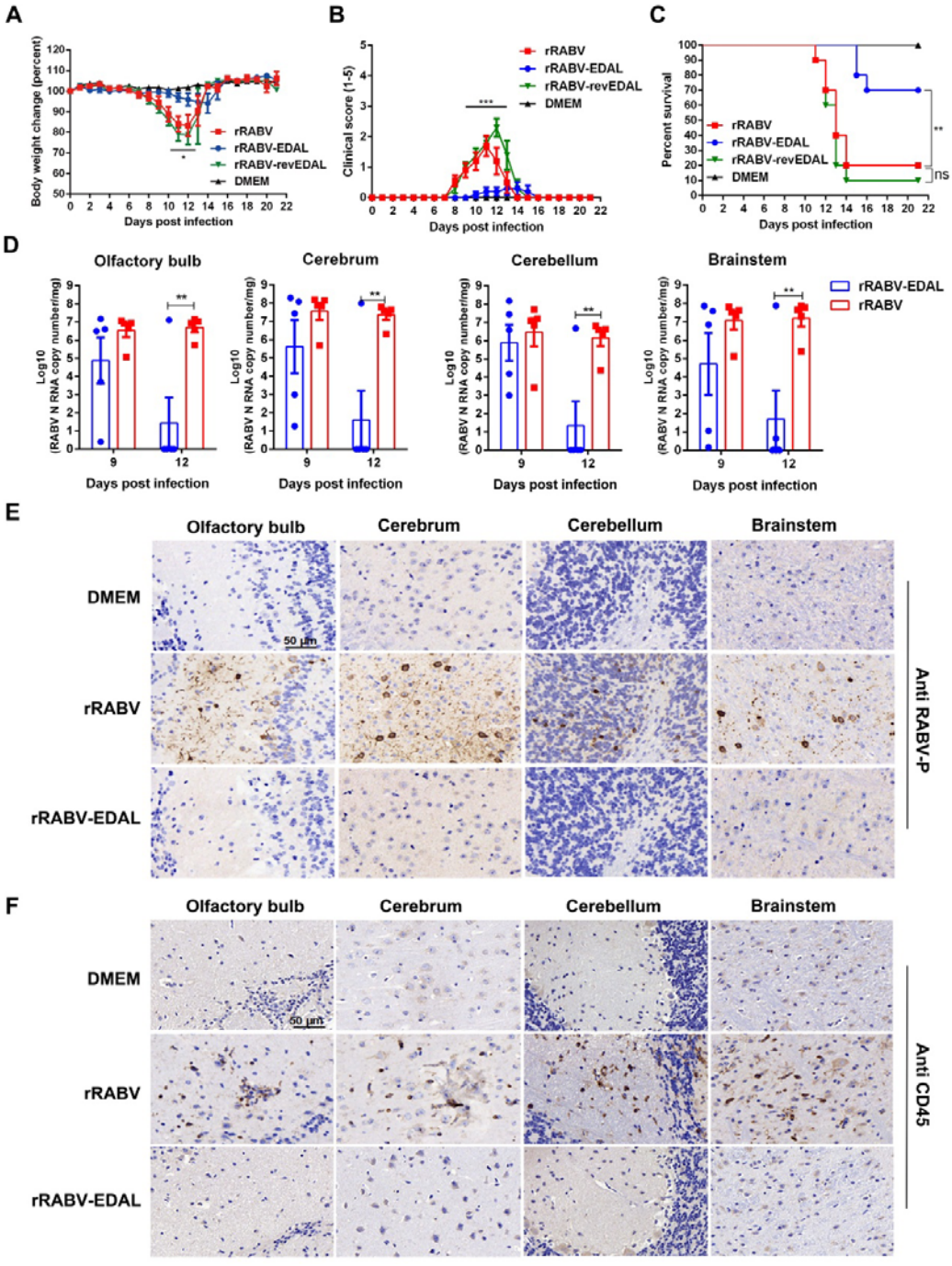

Figure 3. EDAL attenuates RABV pathogenicity *in vivo*.

A,B,C. Female C57BL/6 mice (8-week-old, n=10) were infected intranasally with 100 FFU rRABV, rRABV-EDAL, or rRABV-reEDAL, or mock infected. Body weight change (**A**), clinical score (**B**) and survival ratio (**C**) were

monitored daily for continuous 3 weeks. (means ± SEM; **P<0.01; body weight change and clinical score was analyzed by Two-way ANOVA test; survival ratio was analyzed by log rank test).

D. At indicated time points, the brains from the infected mice were collected for analyzing the level of RABV N mRNA by qPCR. (n=5; means ± SEM; **P<0.01 by student's Two-way ANOVA test).

E,F. At 12 dpi, the brains were collected, resolved by paraffin sections, and analyzed by immunohistochemistry by staining with antibodies against RABV P (**E**) or CD45 (**F**). Scale bar, 50 μm.

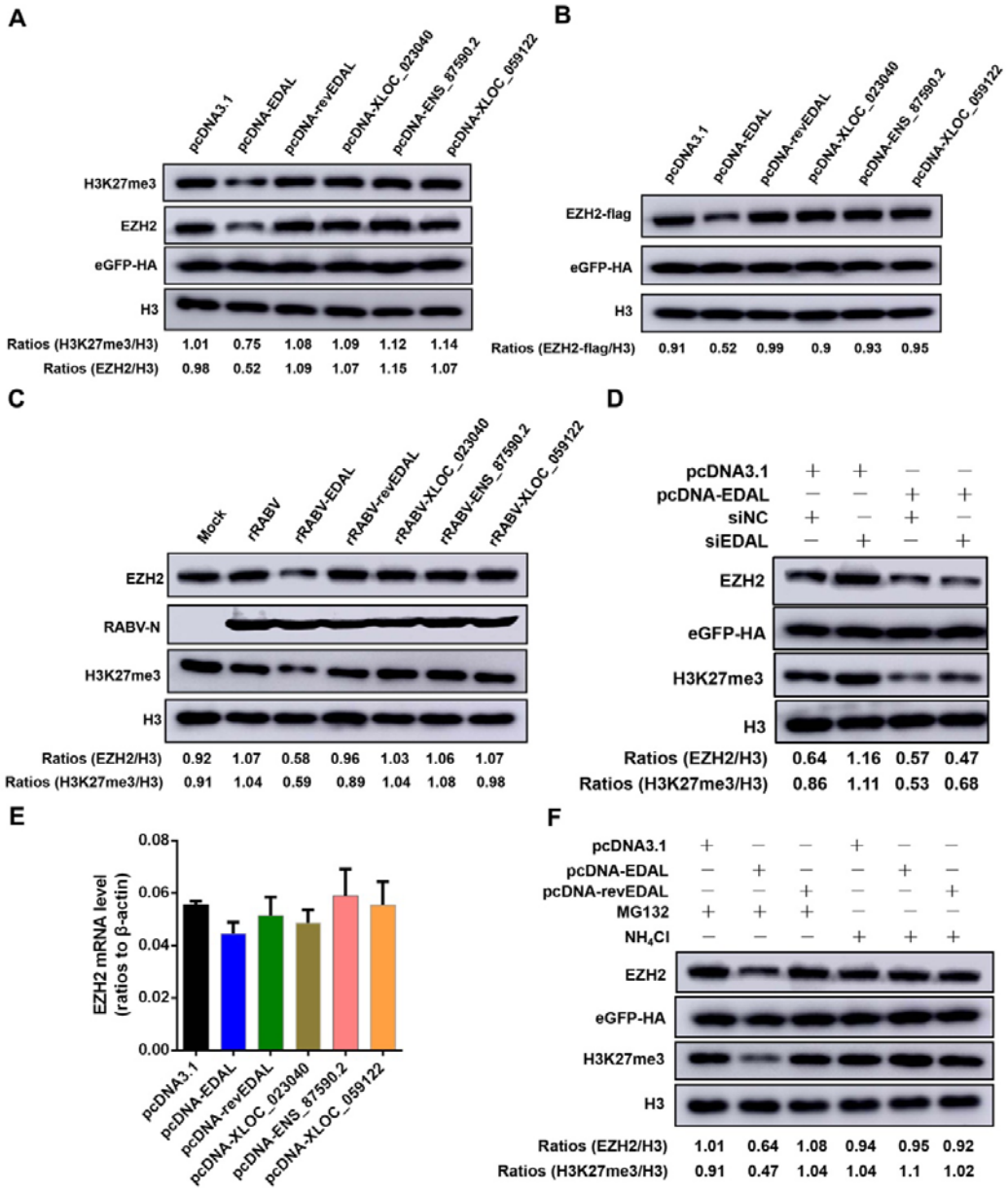

Figure 4. EDAL down-regulates H3K27me3 level by causing the degradation of EZH2.

A. EDAL, reverse EDAL (revEDAL), XLOC_023040, ENSMUSG00000087590.2 (ENS_87590.2) or XLOC_059122 was overexpressed in N2a cells for 48 h and then EZH2 or H3K27me3 level were resolved by Western blotting. The plasmid pCAGGS-eGFP containing a HA tag was used as a transfection control.

B. N2a cells were transfected with pcDNA3.1, pcDNA-EDAL, pcDNA-revEDAL, pcNDA-XLOC_023040, pcDNA-ENS_87590.2, or pcDNA-XLOC_059122, and pCAGGS-EZH2-FLAG and pCAGGS-eGFP-HA (transfection control). EZH2-FLAG levels were measured by Western blotting and normalized to H3.

C. N2a cells were infected with rRABV, rRABV-EDAL, rRABV-revEDAL, rRABV-XLOC_023040, rRABV-ENS_87590.2 or rRABV-XLOC_059122 at MOI 3. At 36 hpi, the EZH2 and H3K27me3 level was resolved by Western blotting and normalized to H3.

D. N2a cells were transfected with siEDAL or siNC (negative control) for 8 h and then transfected with pcDNA3.1 or pcDNA-EDAL. Then EZH2 and H3K27me3 level was resolved by Western blotting and normalized to H3.

E. N2a cells were transfected with pcDNA3.1, pcDNA-EDAL, pcDNA-revEDAL, pcNDA-XLOC_023040, pcDNA-ENS_87590.2, or pcDNA-XLOC_059122. The mRNA levels of EZH2 were analyzed by qPCR. (n=3).

F. pcDNA3.1, pcDNA-EDAL or pcDNA-revEDAL was transfected into N2a cells. The specific inhibitors for proteasome and lysosome, MG132 (10 μM) and NH_4Cl (5 mM), were applied. Then EZH2 and H3K27me3 level was analyzed by Western blotting and normalized to H3.

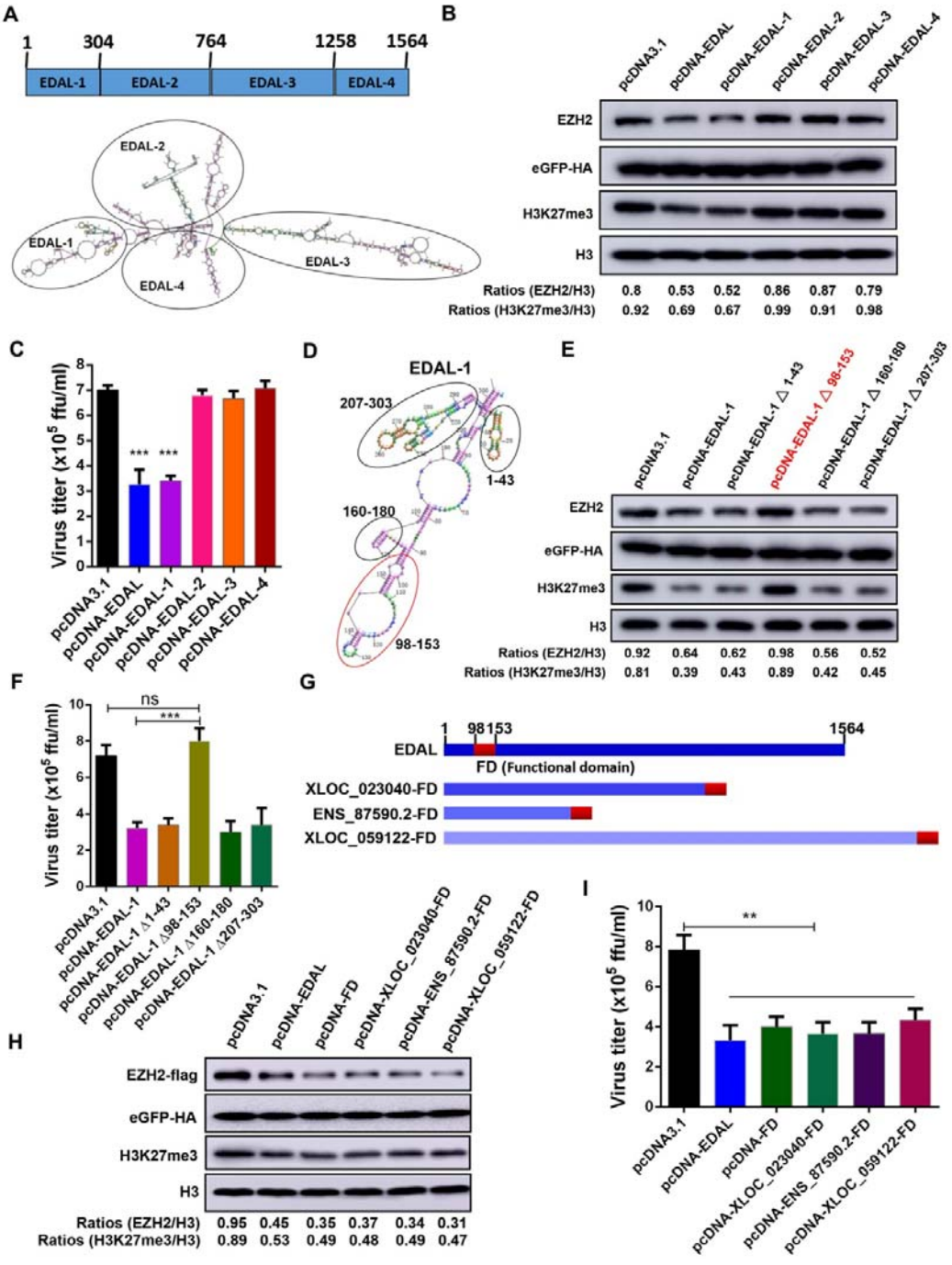

Figure 5. The 56-nt portion of EDAL in 5' end carries the antiviral function.

A. EDAL secondary structure was predicted by RNAstructure Version 5.8 software (http://rna.urmc.rochester.edu/rnastructure.html). EDAL was divided into

four sections based on sub-structures: EDAL-1(1-304 nt), EDAL-2 (305-764 nt), EDAL-3 (765-1258 nt) and EDAL-4 (1259-1564 nt).

B. The full-length EDAL and its truncations were separately transfected into N2a cells for 48 h. The EZH2 and H3K27me3 level was resolved by Western blotting and the ratio normalized to H3 was calculated.

C. The full-length EDAL and its truncations were expressed in N2a cells for 12 h and then the cells were infected with RABV at MOI 0.01. At 48 hpi, the virus titers in the cell supernatant were measured.

D,E. Four sections within EDAL-1 were selected based on the secondary structures (**D**). The four truncations EDAL-1 deleting 1-43 nt (EDAL-1 △1-43), 98-153 nt (EDAL-1 △98-153), 160-180 nt (EDAL-1 △160-180) and 207-303 nt (EDAL-1 △207-303) were cloned into pcDNA3.1, respectively. The different truncations as well as full length EDAL-1 were overexpressed in N2a cells for 48 h. Then EZH2 and H3K27me3 level was resolved by Western blotting and normalized to H3 (**E**).

F. N2a cells were transfected with pcDNA3.1, pcDNA-EDAL-1 or different truncations of EDAL-1 for 12 h. Then the cells were infected with RABV at MOI 0.01 and the virus titers in supernatant were measured at 48 hpi.

G,H. The functional domain (FD) of the 56-nt portion of EDAL was cloned into pcDNA3.1 or fused with 3' end of the other three control lncRNAs (**G**). Then these lncRNAs were transfected together with pCAGGS-EZH2-flag into N2a cells for 48 h. EZH2 and H3K27me3 level were analyzed by Western blotting and normalized to H3 (**H**).

I. N2a cells were transfected with pcDNA3.1, pcDNA-EDAL or different recombinant lncRNAs for 12 h. Then the cells were infected with RABV at MOI 0.01 and the virus titers in supernatant were measured at 48 hpi.

Statistical analysis of grouped comparisons was carried out by student's t test(**P<0.01; ***P<0.001). Bar graph represents means ± SD, *n* = 3.

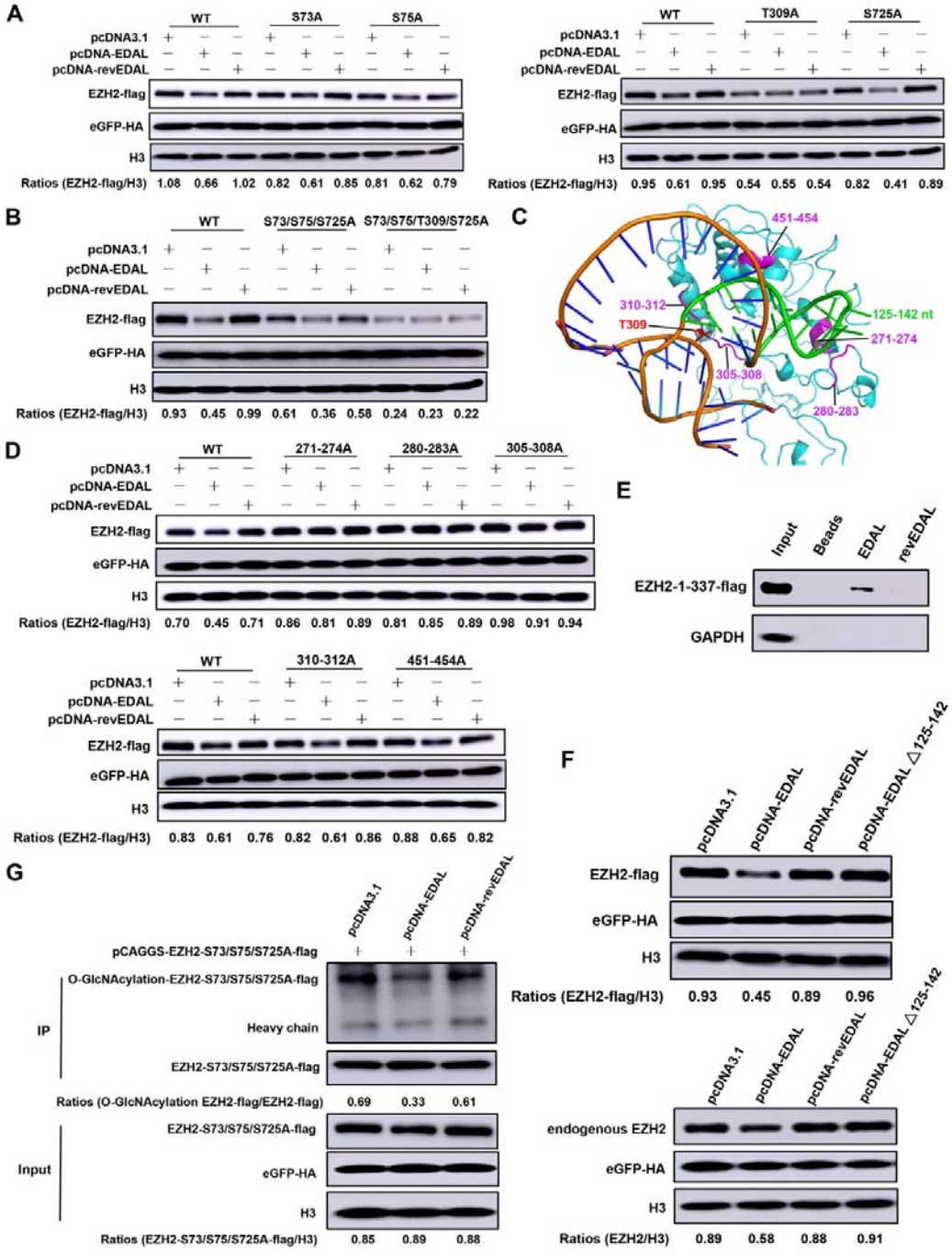

Figure 6. EDAL promotes EZH2 degradation via impeding the

_O_-GlcNAcylation at T309 site.

A. The potential *O*-GlcNAcylation sites of murine EZH2 was individually mutated and expressed together with EDAL or revEDAL in N2a cells for 48 h. Then EZH2 level was analyzed by Western blotting and normalized to H3.

B. The potential *O*-GlcNAcylation sites of murine EZH2 was mutated and co-expressed together with EDAL or revEDAL in N2a cells for 48 h. Then EZH2 level was analyzed by Western blotting and normalized to H3.

C. Murine EZH2 3D structure was predicted with SWISS-MODEL (https://swissmodel.expasy.org/interactive) based on human EZH2 3D structure (PDB code: 5HYN). EDAL-FD 3D structure model was predicted with RNAComposer (http://rnacomposer.ibch.poznan.pl/). The interaction between EDAL functional domain (98-153 nt) and EZH2 was predicted by 3dRPC. The predicted interactional residues among EZH2 were marked with magenta color and among EDAL with green color.

D. The predicted interaction residues of EZH2 were mutated and cloned into pCAGGS vector, and then co-transfected with pcDNA3.1, pcDNA-EDAL or pcDNA-revEDAL in N2a cells for 48 h. Then EZH2 level was analyzed by Western blotting and normalized to H3. The plasmid pCAGGS-eGFP containing a HA tag was used as a transfection control.

E. RNA pull-down analysis of the binding of EDAL or revEDAL to EZH2-1-337-flag.

F. EDAL deleting 125-142 nt (EDAL △125-142) was cloned into pcDNA3.1 (pcDNA-EDAL △125-142). Then pcDNA3.1, pcDNA-EDAL, pcDNA-revEDAL and pcDNA-EDAL △ 125-142 were individually or together with pCAGGS-EZH2-flag transfected into N2a cells for 48 h. Then the overexpressed EZH2 (EZH2-flag) and endogenous EZH2 level was resolved by Western blotting and normalized to H3.

G. The plasmid expressing EZH2-S73/S75/S725A-flag was co-transfected with pcDNA3.1, pcDNA-EDAL or pcDNA-revEDAL in N2a cells and treated with NH_4Cl (5 mM) for 48 h. Then the *O*-GlcNAcylation level of EZH2-S73/S75/S725-flag was analyzed by Western blotting.

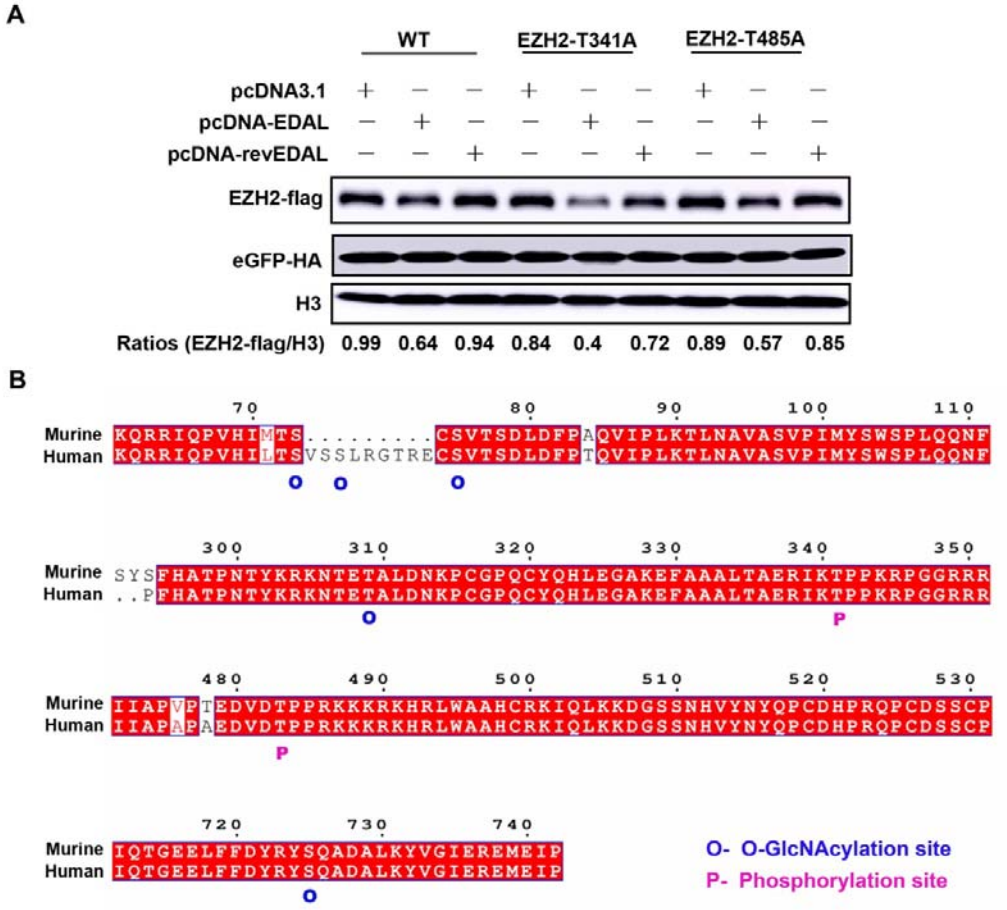

Figure EV4. Amino acid sequence comparison between murine and human EZH2. (Related to Figure 6)

A. The potential phosphorylation sites of murine EZH2 was mutated into A. Then the mutated EZH2 was expressed together with pcDNA3.1, pcDNA-EDAL or pcDNA-revEDAL in N2a cells for 48 h. Then EZH2-flag level was analyzed by Western blotting and normalized to H3.

B. The amino acid sequence of murine and human EZH2 were aligned by using an online software ESPript3.0 (http://espript.ibcp.fr/ESPript/cgi-bin/ESPript.cgi). The *O*-GlcNAcylation sites and phosphorylation sites of human EZH2 were marked by O (*O*-GlcNAcylation) or P (phosphorylation), respectively.

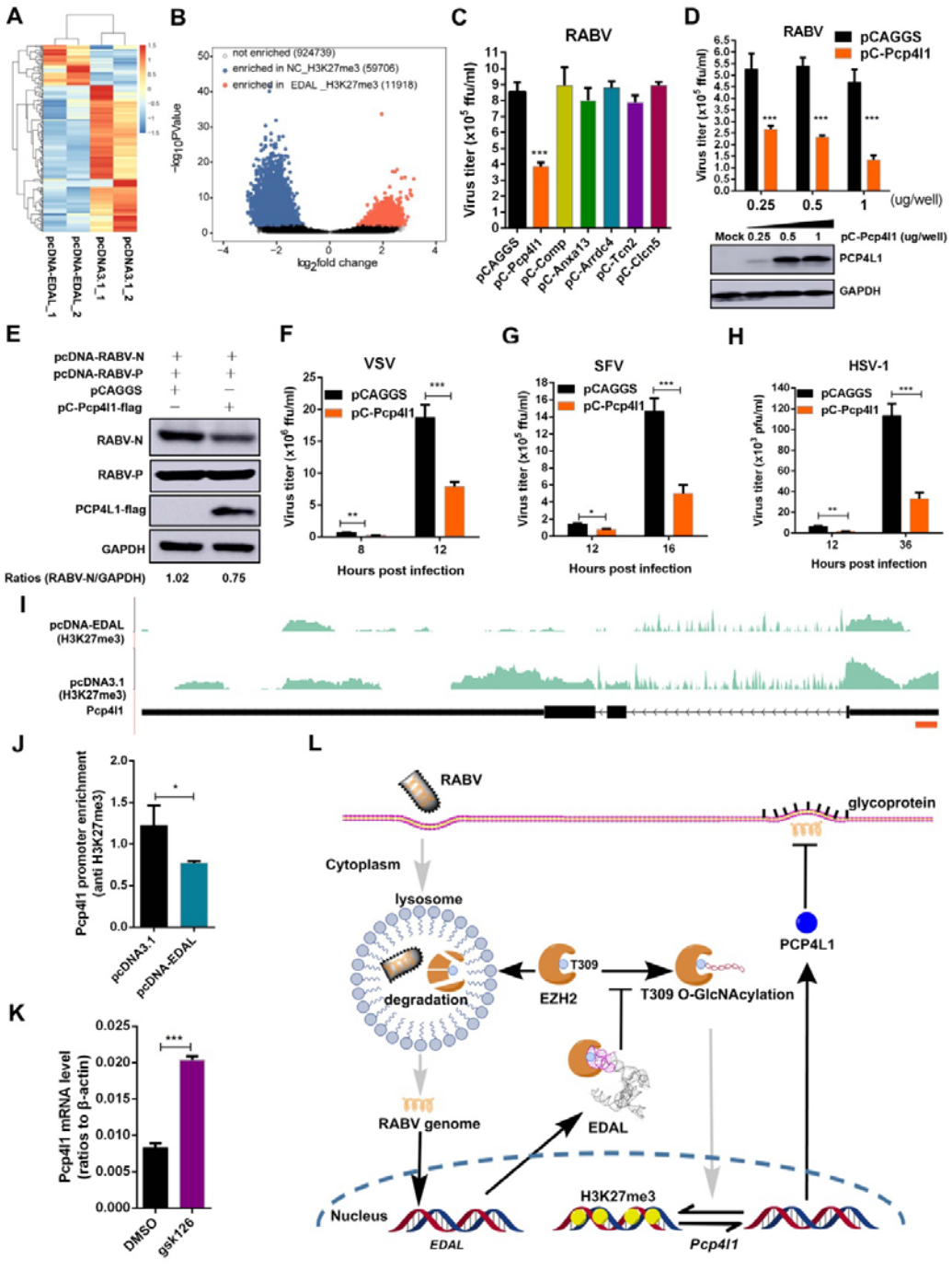

Figure 7. EDAL restricts viral replication by up-regulation of *Pcp4l1*.

A. N2a cells were transfected with pcDNA3.1 or pcDNA-EDAL for 12 h and then infected with RABV at MOI 1 for 48 h. Total RNA was isolated and subjected to RNA-seq analysis (*n*=2; 2 fold change (FC) and 0.01 *p-value*).

B. N2a cells were transfected with pcDNA3.1 or pcDNA-EDAL for 48 h and then ChIP-seq analysis was performed. Volcano plot showed the peaks enriched in negative control (NC) cells and EDAL overexpression cells. X axis was the log2 ratio of EDAL versus NC signals for each peak, and Y axis was the significance of the differences (−log10 (*P-values*)).

C. Six up-regulated and loss of H3K27me3 mark genes were cloned into the mammalian expression vector pCAGGS and overexpressed in N2a cells. At 12 h post transfection, the cells were infected with RABV for 48 h at MOI 0.01, and virus titers in the supernatant were measured.

D. N2a cells were transfected with pCAGGS-*Pcp4l1* (pC-*Pcp4l1*) at indicated dose for 12 h, and then infected with RABV at MOI 0.01. At 48 hpi, the virus load in the cell supernatant was measured. PCP4L1 expression level was analyzed by Western blotting.

E. pcDNA-RABV-N, pcDNA-RABV-P together with pCAGGS or pC-Pcp4l1-flag was transfected into N2a cells for 48 h. The level of RABV-N protein and RABV-P protein was analyzed by Western blotting and normalized to GAPDH.

F. N2a cells were transfected with pCAGGS-*Pcp4l1* (pC-*Pcp4l1*) for 12 h, and then infected with VSV at MOI 0.01. At indicated hpi, the virus load in the cell supernatant was measured.

G. N2a cells were transfected with pC-*Pcp4l1* for 24 h, and then infected with SFV at MOI 0.01. At indicated hpi, the virus load in the cell supernatant was measured.

H. N2a cells were transfected with pC-*Pcp4l1* for 24 h, and then infected with HSV-1 at MOI 0.01. At indicated hpi, the virus load in the cell supernatant was measured.

I. Sequencing profile of *Pcp4l1* for ChIP-seq. The two tracks show H3K27me3 signals for pcDNA3.1 and pcDNA-EDAL samples after removing input background. The brown rectangle indicates the predicted promoter region of *Pcp4l1*.

J. N2a cells were transfected with pcDNA-EDAL or pcDNA3.1 for 48 h, and then ChIP-qPCR were performed with H3K27me3 antibody in the promoter region of *Pcp4l1*.

K. N2a cells were treated with 4 μM gsk126 or DMSO (mock) for 48 h and *Pcp4l1* mRNA level was analyzed by qPCR.

L. Proposed model for EDAL-induced EZH2 lysosomal degradation, and the potential subsequent impact on EZH2-mediated epigenetic silencing of *Pcp4l1.*

Statistical analysis of grouped comparisons was carried out by student's t test(**P<0.01; ***P<0.001). Bar graph represents means ± SD, *n* = 3.

Supplementary Information for

A novel antiviral lncRNA EDAL shields a T309 *O*-GlcNAcylation site to promote EZH2 degradation

Baokun Sui, Dong Chen, Wei Liu, Qiong Wu, Bin Tian, Jing Hou, Yingying Li, Shiyong Liu, Juan Xie, Hao Jiang, Zhaochen Luo, Lei Lv, Fei Huang, Ruiming Li, Min Cui, Ming Zhou, Huanchun Chen, Zhen F. Fu, Yi Zhang, Ling Zhao

Corresponding authors:

Ling Zhao, Mailing address: State Key Laboratory of Agricultural Microbiology, Huazhong Agricultural University, Wuhan, 430070, China. E-mail: zling604@yahoo.com

Yi Zhang, Mailing address: Center for Genome analysis and Laboratory for Genome Regulation and Human Health, ABLife Inc., Wuhan, 430075, China. E-mail: yizhang@ablife.cc

This file includes:

Appendix Figures S1 to S2

Appendix Tables S1 to S2

Supplementary Figures

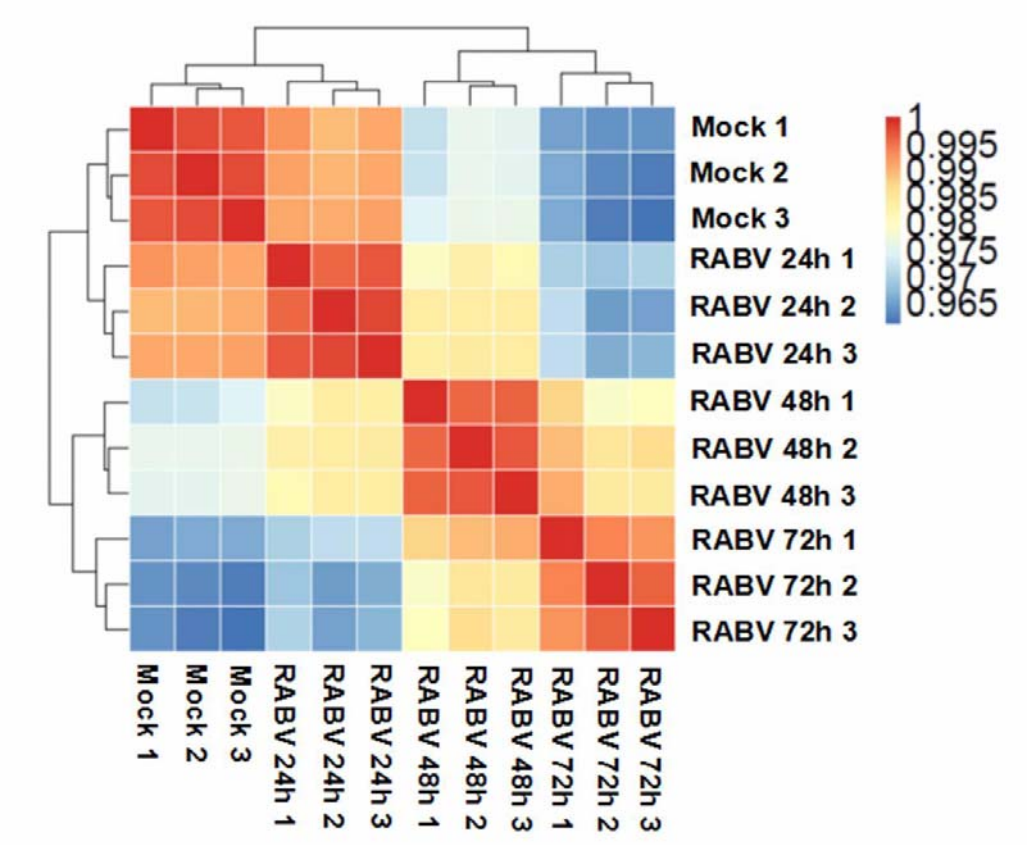

Appendix Figure S1. Sample correlation analysis. Hierarchical clustering heatmap shows global transcriptional changes after RABV infection. The Pearson correlation coefficients (PCCs) for each sample pair are represented using the colors in the color bar to indicate coefficient magnitude.

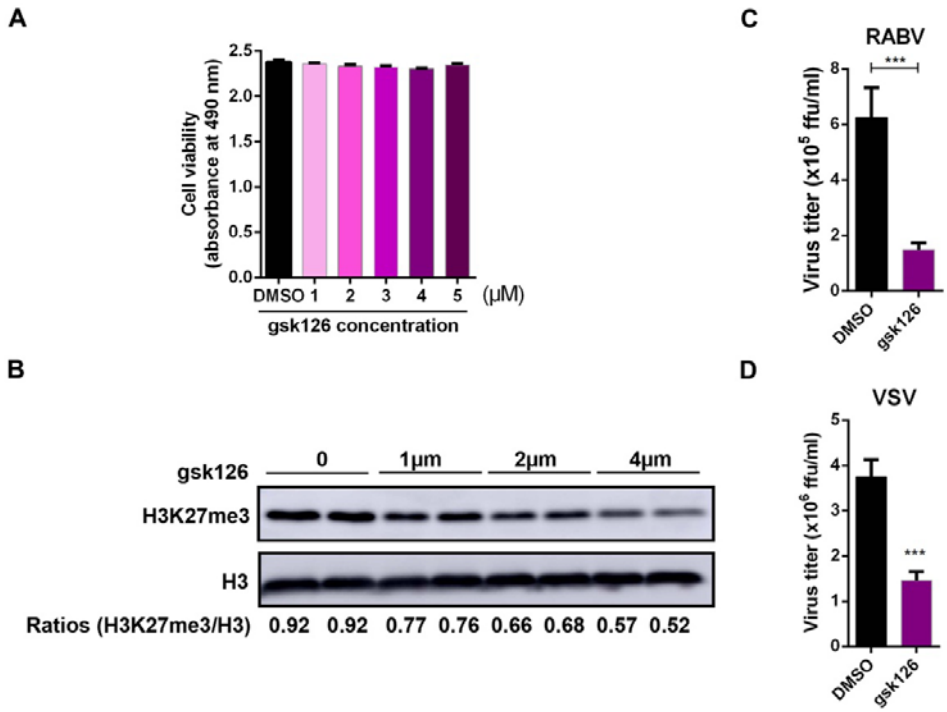

Appendix Figure S2. EZH2 specific inhibitor gsk126 inhibits RABV and VSV replication in N2a cells.

A,B. After treatment with different concentrations of gsk126, an EZH2 specific inhibitor, the viability of N2a cells was evaluated by using Cell Titer 96 AQueous One Solution cell proliferation assay kit (Promega, Madison, WI) (**A**). (n=3) H3K27me3 levels were measured by Western blotting and normalized to H3 (**B**).

C. N2a cells were treated with 4 μM gsk126 or DMSO for 12 h, and then infected with rRABV at MOI 0.01. At 48 hpi., the virus load in the supernatant was titrated.

D. N2a cells were treated with 4 μM gsk126 or DMSO for 12 h, then infected with VSV at MOI 0.01 for 12 h, the virus load in the supernatant were measured.

Statistical analysis of grouped comparisons was carried out by student's t

test(***P<0.001). Bar graph represents means ± SD, *n* = 3.

Supplementary tables.

Appendix Table S1. Sequencing and mapping information of ChIP-seq experiments. Each sample was tested in duplicates.

Sample	Raw reads	Reads after QC	total mapped reads	uniquely mapped reads	multiple mapped reads
pcDNA3.1_H3K27me3_1	69932858	55668777	52437993 (94.20%)	39942525 (76.17%)	12495468 (23.83%)
pcDNA3.1_H3K27me3_2	67891278	45142907	42187626 (93.45%)	30301699 (71.83%)	11885927 (28.17%)
pcDNA3.1_input_1	78994340	65958160	63686273 (96.56%)	46843529 (73.55%)	16842744 (26.45%)
pcDNA3.1_input_2	76318976	55917681	53343077 (95.40%)	38161225 (71.54%)	15181852 (28.46%)
pcDNA-EDAL_H3K27me3_1	73941712	58906209	55816652 (94.76%)	40379662 (72.34%)	15436990 (27.66%)
pcDNA-EDAL_H3K27me3_2	68085768	45952519	42358792 (92.18%)	31024033 (73.24%)	11334759 (26.76%)
pcDNA-EDAL_input_1	72335164	59681813	57346675 (96.09%)	41376294 (72.15%)	15970381 (27.85%)
pcDNA-EDAL_input_2	70565824	51660023	49080890 (95.01%)	35607692 (72.55%)	13473198 (27.45%)

1561 **Appendix Table S2.** The primer sets used in this study.

qPCR primer name	Sequence(5'-3')
XLOC_059122-F	GCTGTGGGGCATTTTCTCAA
XLOC_059122-R	AGCAGGTCAGGAATCAAGAG
ENSMUSG00000087684-F	CTGTGTCTTGGCTTGGGAGT
ENSMUSG00000087684-R	CCTGGGTGTTTCCTTTCTCA
XLOC_050868-F	GTCAGCCCTCTCTTTCCGCC
XLOC_050868-R	GCCTCCTGCTCTTCACGCTC
ENSMUSG00000085744-F	AGGGTCTCTGCCTGGAACT
ENSMUSG00000085744-R	AGTGGATGCTTTGTGAGG
XLOC_005934-F	AGTCTCCTGGGTGTTTGTGG
XLOC_005934-R	TGTGATGTCCCCTTGTGATG
XLOC_023040-F	CCAGTTTGGGAGGGGAGGAC
XLOC_023040-R	ATGGGTGTTGCGGATGGTG
XLOC_026667-F	AAATGGAAACCGAGGGTGGG
XLOC_026667-R	ATTGAGGGGCTGGGATGTGA
XLOC_047835-F	GGGAACCAGAGACAACGGGA
XLOC_047835-R	GCTGCTCCTGCCCACCATT
XLOC_058596-F	AGTAGGGCAGTGTTTGGCAC
XLOC_058596-R	GGCAGGTGGATTTCTGAGTT
Mouse β-Actin-F	CACTGCCGCATCCTCTTCCTCCC
Mouse β-Actin-R	CAATAGTGATGACCTGGCCGT
Mouse EDAL-F	GTCCCTGTGTGGGTTACTGG
Mouse EDAL-R	TGGGGCTTACTTCCTTTCTG
RABV N mRNA-F	GATCGTGGAACACCATACCC
RABV N mRNA-R	TTCATAAGCGGTGACGACTG
Mouse Pcp4l1-F	ACACCAAAACACCTCCAGCA

Mouse Pcp4l1-R	CCTCCTCGGCCTTCTTGATG

1562

1563

ChIP-qPCR primer name	Sequence(5'-3')
Mouse Pcp4l1-F	TCCCGCTCTCTCCGTCTTA
Mouse Pcp4l1-R	GCCTCCAGCCCAACCAATA

1564

Primers for clone	Sequence(5'-3')
PpcDNA-EDAL-F	CTCACTATAGGGAGACCCAAGCTGGCTA GCTGGAGGCATTTTCTGAG
PpcDNA-EDAL-R	CGAGGCTGATCAGCGGGTTTAAACGGG CCCTGTGTTTGTTAAAATAC
PpcDNA-XLOC_059122-F	CTCACTATAGGGAGACCCAAGCTGGCTA GCCAATCCCCAATCTGTAG
PpcDNA-XLOC_059122-R	CGAGGCTGATCAGCGGGTTTAAACGGG CCCCTAACTGAGGAAATGCC
PpcDNA-ENSMUSG00000085744-F	CTCACTATAGGGAGACCCAAGCTGGCTA GCCCACATACTGAATCTGA
PpcDNA-ENSMUSG00000085744-R	CGAGGCTGATCAGCGGGTTTAAACGGG CCCCCGCCTTGGGGGCATAT
PpcDNA-XLOC_23040-F	CTCACTATAGGGAGACCCAAGCTGGCTA GCTCTATGTGAGGACACTTC
PpcDNA-XLOC_23040-R	CGAGGCTGATCAGCGGGTTTAAACGGG CCCTGCTCTGAAGCCTATGAA
PpcDNA-ENSMUSG00000103464.1-F	CTCACTATAGGGAGACCCAAGCTGGCTA GCGTTCAATAAAACTTTGGT
PpcDNA-ENSMUSG00000103464.1-R	CGAGGCTGATCAGCGGGTTTAAACGGG CCCCCGCGGCAAAAGCTTTAT
PpcDNA-ENSMUSG00000087590.2-F	CTCACTATAGGGAGACCCAAGCTGGCTA GCTTTCTATGCTCGCACGCA

PpcDNA-ENSMUSG00000087590.2-R	CGAGGCTGATCAGCGGGTTTAAACGGGCCCGAACAGCACATCGAAGCA
PrRABV-EDAL-F	CATGAAAAAAACTAACACTCCTCCCGTACGTGGAGGCATTTTCTGAG
PrRABV-EDAL-R	TACAGTTTTTTTCTCGACTGAAATGCTAGCTGTGTTTGTTAAAATAC
PrRABV-reEDAL-F	CATGAAAAAAACTAACACTCCTCCCGTACGTGTGTTTGTTAAAATAC
PrRABV-reEDAL-R	TACAGTTTTTTTCTCGACTGAAATGCTAGCTGGAGGCATTTTCTGAG
PpCAGGS-EZH2-flag-F	GCCACCATGGACTACAAAGACGATGACGACAAGGGCCAGACTGGGAAG
PpCAGGS-EZH2-flag-R	CTCGAGTTACTTGTCGTCATCGTCTTTGTAGTCAGGGATTTCCATTTC
PpCAGGS-Comp-F	TTGTGCTGTCTCATCATTTTGGCAAAGAATTCGCCACCATGGGCCCCACTGCCTGCGTTCT
PpCAGGS-Comp-R	TGGCAGAGGGAAAAAGATCTGCTAGCTCGAGTTAGACTCTCTGCAGCCGGTGAC
PpCAGGS-Anxa13-F	TTGTGCTGTCTCATCATTTTGGCAAAGAATTCGCCACCATGGGGAATCGTCATGCCAAAGA
PpCAGGS-Anxa13-R	TGGCAGAGGGAAAAAGATCTGCTAGCTCGAGTTAGTGCAAGAGAGCTACCAGCA
PpCAGGS-Arrdc4-F	TTGTGCTGTCTCATCATTTTGGCAAAGAATTCGCCACCATGGGAGGCGAGGCGGGAGCCGA
PpCAGGS-Arrdc4-R	TGGCAGAGGGAAAAAGATCTGCTAGCTCGAGTTAGAGAATGAAGGATACAGGCT
PpCAGGS-Tcn2-F	TTGTGCTGTCTCATCATTTTGGCAAAGAATTCGCCACCATGGAGCTCCTGAAGGCGCTGCT

PpCAGGS-Tcn2-R	TGGCAGAGGGAAAAAGATCTGCTAGCTC GAGTTACCATCTAACTAGCCGCAGCT
PpCAGGS-Clcn5-F	TTGTGCTGTCTCATCATTTTGGCAAAGAA TTCGCCACCATGGCCATGTGGCAGGGA GCCAT
PpCAGGS-Clcn5-R	TGGCAGAGGGAAAAAGATCTGCTAGCTC GAGTTAGTTGAAGAGAATGGAATCAG
PpCAGGS-Pcp4l1-F	GAATTCGCCACCATGAGCGAGCTTAACA CCAAAAC
PpCAGGS-Pcp4l1-R	CTGCTAGCTCGAGTTAGGAGCTGGAATC CTTTTTCC

1565